Applied Thermal Engineering 249 (2024) 123275

Contents lists available at ScienceDirect

Applied Thermal Engineering

journal homepage: www.elsevier.com/locate/apthermeng

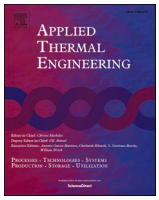

Research Paper

Initial experimental testing of a hybrid solar-dish Brayton cycle for combined heat and power (ST-CHP)

Jonathan K. Swanepoel [a], Willem G. le Roux [a,*], Casey Roosendaal [a], Seyed H. Madani [b], Gideon de Wet [a,c], Theoklis Nikolaidis [d], Westley Roosendaal [a], Chase Onorati [a], Adriano Sciacovelli [e], Yize Liu [d], Tlou S. Mokobodi [a], Duncan S. McGee [a], Ken J. Craig [a]

[a] Department of Mechanical and Aeronautical Engineering, University of Pretoria, Hatfield, Pretoria, 0028, South Africa
[b] Samad Power Ltd., Milton Keynes, MK11 3JB, United Kingdom
[c] SimGenics Pty Ltd, Waterkloof Glen, Pretoria, 0010, South Africa
[d] Centre for Propulsion and Thermal Power Engineering, School of Aerospace Transport and Manufacturing (SATM), Cranfield University, Cranfield, MK43 0AL, United Kingdom
[e] School of Chemical Engineering, University of Birmingham, Birmingham, B15 2TT, United Kingdom

ARTICLE INFO

Keywords:
Brayton cycle
Cavity receiver
Solar dish
Micro gas turbine
Thermal Storage
Renewable Energy

ABSTRACT

The Solar Turbo Combined Heat and Power (ST-CHP) project developed a novel solar-gas hybrid prototype for combined heat and power generation in Pretoria, South Africa. A vacuum-membrane faceted parabolic dish with a large-pipe open-cavity receiver was coupled to a counterflow recuperator, a combustion chamber, a micro gas turbine with air bearings and a phase change thermal energy storage unit containing solar salts. This study aimed to validate the electrical output of the full-scale dish-Brayton prototype, addressing the literature gap on micro-scale dish-Brayton plants' in-field power generation. Solar hybridization of micro gas turbine technology can significantly reduce combustion fuel consumption. A performance analysis under relevant conditions revealed a late afternoon micro gas turbine output intermittently peaking at 0.4 kWe and subsequently stabilizing to a steady state of 0.145 kWe at 130 krpm. A SimuPact numerical model and an analytical model supplemented the telemetry data to reduce interference in the experimental setup and fully characterize the ST-CHP prototype performance, estimating a steady-state turbine isentropic efficiency of 57%, a compressor efficiency of 71% and a collector efficiency of 17% due to the late afternoon steady-state point. Analytical case studies revealed that fuel savings of between 12% and 33% at the combustion chamber were achievable from the solarized preheating. A subsequent test of the micro gas turbine without solar hybridization or a recuperator resulted in 1.05 kWe being generated. The study confirms the dish-Brayton prototype's viability for combined heat and power generation, producing an initial full-scale performance characterisation during in-field testing, and highlighting the impact of solar hybridization on turbine electrical output. Optical efficiency, insulation effectiveness, pressure losses, and turbine operating conditions were identified as critical areas requiring optimization to improve electrical output. The lessons learned, and the calibrated numerical model may be used to optimize the performance of the dish-Brayton plant in future work. The successful in-field full-scale power generation of the ST-CHP prototype adds to the available literature on dish-Brayton technology and brings the technology closer to a commercial product.

1. Introduction

1.1. Background and motivation

The world has seen a steady increase in the utilisation of renewable energy power generation resources with roughly 300 GW of global renewable energy added in 2022, however, this is still far from the annual target of 1000 GW [1]. The use of concentrated solar power (CSP) as a renewable energy source constitutes concentrating and capturing the solar radiation emitted by the sun and transforming it into electricity and useful process heat. The heat is transformed into an electrical output using turbine or Stirling technology and electrical generator units [2]. A global combined annual capacity of 17622 GWh was estimated to be generated by the operational CSP plants in the form of electricity in 2023 [3], and a key interest that is being established in

* Corresponding author.
E-mail address: willem.leroux@up.ac.za (W.G. le Roux).

https://doi.org/10.1016/j.applthermaleng.2024.123275
Received 1 December 2023; Received in revised form 11 April 2024; Accepted 25 April 2024
Available online 26 April 2024
1359-4311/© 2024 The Author(s). Published by Elsevier Ltd. This is an open access article under the CC BY-NC license (http://creativecommons.org/licenses/by-nc/4.0/).

Nomenclature

Symbols

A	Area, (m^2)
$\bar{A}$	Coefficient, (-)
$\bar{B}$	Coefficient, (-)
c	Critical heat capacity ratio, (-)
C	Heat capacity, (W/K)
Cp	Pressure coefficient, (-)
D	Diameter, (m)
$\dot{E}$	Electrical output, (W)
h	Specific enthalpy, (J/kg)
$\hat{h}$	Convection heat transfer coefficient, (W/m^2K)
I	Irradiance, (W/m^2)
k	Conductivity, (W/mK)
L	Length, (m)
$\dot{m}$	Mass flow rate, (kg/s)
N	Number of items, (-)
Nu	Nusselt number, (-)
p	Perimeter, (m)
P	Pressure, (Pa)
$\dot{Q}$	Heat transfer, (W)
R	Thermal resistance, (K/W)
Re	Reynolds number, (-)
t	Thickness, (m)
T	Temperature, (K)
U	Heat transfer coefficient, (W/m^2K)
V	Velocity, (m/s)
$\dot{V}$	Volumetric flow rate, (m^3/s)
$\dot{W}$	Mechanical work, (W)

Subscripts

1–13	Station number (Fig. 1)
air	Air
amb	Ambient
ap	Aperture
b	Bulk fluid temperature
cap	Captured
cav	Cavity
channel	Channel
coil	Receiver coil
col	Collector
cold	Cold side
comb	Combustion chamber / combustion
cond	Conduction
conv	Convection
eff	Effective
f	Fuel
flange	Pipe flange
forced	Forced convection
h	Hydraulic diameter
i	Increment / Inner
inner	Inner
ins	Insulation
int	Intercepted
loss	Heat loss
mchannel	Micro-channel
min	Minimum
natural	Natural convection
net	Net
o	Outer
OD	Flange outer diameter / flange lip
outer	Outer
output	Output
pr	Propane
rad	Radiation
r	Receiver
recup	Recuperator
ref	Reflector
s	Surface / heat transfer area
shaft	MGT shaft work
side	Recuperator hot or cold side
slpm	Standard litres per minute
STP	at STP conditions
sun	Sun
th	Thermal
th-el, MGT	MGT thermal to electrical
tot	Total
tube	Exposed tubing surface
T	Turbine

Greek

γ	Intercept factor
Δ	Change
ε	Emissivity
$\breve{\varepsilon}$	Effectiveness
η	Efficiency
μ	Viscosity, (Pa.s)
ρ	Density, (kg/m^3)
$\bar{\rho}$	Reflectivity, (-)
Π	Dimensionless group
ω	MGT speed, (krpm)
σ	Stefan Boltzmann constant, (W/m^2K^4)

Acronyms

CAD	Computer Aided Design
CHP	Combined Heat and Power
CSP	Concentrated Solar Power
DAQ	Data Acquisition system
DNI	Direct Normal Irradiance
EUF	Energy Utilization Factor
HMI	Human Machine Interface
LHV	Lower heating value
LPG	Liquified Petroleum Gas
MGT	Micro-Gas Turbine
NREL	National Renewable Energy Laboratory
NTU	Number of Transfer Units
PID	Proportional-Integral-Derivative
POI	Point of Interest
PSU	Power Supply Unit
PV	Photovoltaic
QTP	Quick Time Performance
SAURAN	South African Universities Radiometric Network
ST-CHP	Solar Turbo-Combined Heat and Power
STP	Standard Temperature and Pressure
TES	Thermal Energy Storage

the concentrated solar thermal industry is the use of concentrated solar heat for the use of industrial thermal manufacturing processes [4–6].

Based on 2022 research data collected by Thonig et al. [3] and SolarPACES [7], large-scale parabolic trough collectors and solar power towers were the prominent CSP plant configurations operating on Rankine or organic Rankine cycles of the 114 plants in operation globally to provide bulk electricity supply. Small-scale cogeneration CSP solutions are growing in interest due their compact design resulting in a solution for dispatchable heat and power to remote locations [8–10]. Mills [11] argued that there will be a growing interest in smaller, modular CSP systems which will be incorporated into existing CHP solutions near city centres. Fresnel reflectors, parabolic troughs and parabolic dishes were listed as the ideal solutions [11]. Coventry and Andraka [12] and Aichmayer et al. [13] stated that dish CSP is ideal for integrating with MGT technology because of its high concentration ratios, allowing for efficient heat transfer at high temperature and efficient integration with micro gas turbine technology. An open dish-Brayton cycle with air as the working fluid is beneficial at small-scale due to the simplicity of the design (with the exception of the MGT), and the collector's ability to reach higher process temperatures for process heat applications [14]. Dish CSP also provides power at a smaller scale than heliostat CSP which has benefits in commercial scalability in meeting the needs of distributed power generation as well as large scale mass-manufactured projects [15]. Recuperated dish-Brayton plant solar-to-mechanical efficiencies of between 10 % and 20 % where theoretically estimated, and increased up to 21 % when high-temperature phase change thermal storage was incorporated into the receiver cavity [15,16]. Solar Brayton cycles have typically realized competitive power generation efficiencies at larger scale power outputs and successful demonstration plants have been operated at this scale using heliostat field solar concentration technology [17–19], however there is a lack in publicized work on successful demonstrations (regarding an electrical output) of dish-Brayton plants.

From the literature available, only two full-scale demonstrations of dish-Brayton plants have been published [12]. The first (and only) successful, full-scale demonstration achieving an electrical output was conducted in the 1980′s by Sanders Associates and Garret AiResearch [20–22]. An electrical output of between 0.4 kWe and 2.9 kWe was achieved using a 44 m^2 to 49 m^2 dish for sun-only and a hybrid configuration fuelled by methane. The second full-scale sun-only demonstration of a dish-Brayton plant was conducted at the end of the OmSOP project in 2017, but the plant failed to produce an electrical output [13,23–31]. Temperature limits on the oil bearings used in the OmSOP MGT caused the plant to only produce a decoupled shaft work of between 0.5 kW and 0.9 kW. Following the closure of the OmSOP project in 2017, publications were produced regarding the performance prediction and optimization of the OmSOP plant [32–34]. Other notable attempts of full-scale power production have been made such as the SolarCAT project carried out by Brayton and Southwest Solar Technologies 2011 [35], but the available published work shows that the project did not proceed beyond modular experimental testing of subassemblies. Further detail on solar thermal Brayton cycle full-scale testing is summarised in Table 1 and Table 2.

Table 1
Summary of solar Brayton full-scale testing.

ID	Company / Project	Type	Recuperated	Period	Ref.
1	Sanders Associates	Dish-Brayton	Yes	1982–1984	[20–22]
2	Capstone Microturbine	Heliostat Brayton	–	2010	[17]
3	Solugas	Heliostat Brayton	No	2012–2013	[18,19]
4	OMSoP	Dish-Brayton	Yes	2013–2017	[13,23–31]

Table 2
Summary of full-scale testing results of solar Brayton power projects.

ID (refer to Table 1):	1a	1b	2	3	4
Hybrid/Sun-only	Hybrid	Sun-only	Sun-only	Hybrid	Sun-only
Direct Normal Irradiance, I_{sun} (W/m^2)	805	950	825	949–1020	>800
Wind speed, (km/h)	–	–	–	3.4–24.2	–
Reflective area, A_{ref} (m^2)	43.8	49.3	–	–	96.14
Air mass flow rate, $\dot{m}_{air}$ (g/s)	87	77	41	5600–5700	–
Fuel mass flow rate, $\dot{m}_f$ (g/s)	0.74	0	0	–	0
Fuel type	methane	N/A	N/A	methane	N/A
Receiver inlet temperature, $T_{r,in}$ (°C)	650.3	550	542	–	–
Receiver outlet temperature, $T_{r,out}$ (°C)	796.0	779	871	602–801	–
Average cavity temperature, T_{cav} (°C)	875.0	843	–	–	–
Turbine inlet temperature, $T_{T,in}$ (°C)	870.2	683	–	–	100–270
Turbine outlet temperature, $T_{T,out}$ (°C)	711.7	601	–	–	–
Reflected heat, $\dot{Q}_{ref}$ (kW)	30.1	38.74	173.83	–	>76.91
Receiver heat captured, $\dot{Q}_{cap}$ (kW)	14.5	19.9	155.14	1751–4006	–
Combustion heat, $\dot{Q}_{comb}$ (kW)	36.3	0	–	–	–
MGT shaft work, $\dot{W}_{shaft}$ (kW)	4.4	–	–	–	0.5–0.9
MGT electrical output, $\dot{E}_{out}$ (kWe)	2.9	0.41	24.04	1855–3561	–
Collector thermal efficiency,$\eta_{th,col}$	0.35	–	0.11	–	–
Receiver thermal efficiency,$\eta_{th,r}$	0.57	0.66	0.89	0.68–0.78	–
MGT thermal to electrical efficiency,$\eta_{th-el,MGT}$	0.06	–	0.16	–	–

Studies conducted at the University of Pretoria between 2013 and 2014 designed a small-scale open-cavity solar receiver to be used in a solar-dish Brayton cycle through a holistic plant entropy generation minimization technique [14,16,36]. A relatively large inner tube diameter of 0.0833 m for the receiver coil was shown to benefit the entire dish-Brayton cycle due to the lower pressure drop, benefiting the performance of the downstream MGT. In-cavity, high-thermal-conductivity, phase-change thermal storage receiver configurations were explored [15], and multiple studies have been conducted to analytically and experimentally characterise heat loss from the receiver cavity [16,37,38]. Additionally, a novel low-cost vacuum membrane facetted dish reflector was developed at the University of Pretoria with a target intercept factor of 90 % at a geometric concentration ratio of 396 [39–41].

According to the literature, only two full-scale demonstrations of power generation using a dish-Brayton cycle have been published, namely, the experimental study by Sanders Associates & Garret AiResearch in the 1980′s [20–22] and the OMSoP project in 2017 [13,23–31]. The lack of literature available regarding full-scale dish-Brayton on-sun testing shows the need for further experimental research in this field. A recuperated solar-dish Brayton prototype was designed and built at a demonstration level to conduct full-scale, on-sun,

naturalistic, testing at the University of Pretoria, South Africa (at an elevation of about 1380 m). The Brayton cycle contained a solar collector with a helically-coiled open-cavity tubular solar receiver, an LPG combustion chamber, a micro gas turbine, a recuperator, and a solar salt thermal energy storage unit. The MGT was manufactured by Samad Power Ltd and operated on an air bearing design to minimize frictional losses. A multi-faceted, vacuum membrane dish solar collector was used to preheat the air reducing fuel consumption in the LPG-fuelled combustion chamber. The electrical output was directed to an island-style micro-grid that allowed for accurate monitoring of charge and discharge of the power cycle. The primary purpose of the experimental study was to demonstrate a proof of concept with the dish-Brayton prototype successfully generating electricity during field testing. Solar hybridization of micro gas turbine technology has the potential to significantly reduce combustion fuel at the combustion chamber. Naturalistic field testing exposes the dish-Brayton prototype to a transient environment that does not coincide with lab-controlled tests and is a key milestone in developing the technology readiness level towards a commercialised product. Secondary objectives were to characterise performance of the sub-assemblies within the dish-Brayton prototype in relation to one another and make recommendations to progress the technology. A SimuPact numerical investigation was conducted to supplement the telemetry data and fully characterise the performance of the dish Brayton prototype.

1.2. Novelty and contributions

The novelty of this work is based on the following contributions:

- The distinct combination of sub-assembly technologies (as listed below) integrated into the dish-Brayton prototype, and the successful full-scale demonstration of power generation during on-sun field tests:
  - o Multi-faceted vacuum membrane parabolic dish reflector
  - o Helically-coiled, large-tube, open-cavity receiver
  - o Micro gas turbine operating on air bearings at a 1 kWe scale
  - o LPG-fuelled combustion chamber
  - o Counterflow recuperator
  - o Phase change thermal energy storage using solar salts
  - o Island-style microgrid
- Full-scale, in-field experimental analysis producing a realistic performance characterisation between sub-assemblies and a performance characterisation of the entire dish-Brayton prototype exposed to naturalistic environmental conditions.

2. Experimental setup

The process flow diagram and a SolidWorks model of the ST-CHP prototype is presented in Fig. 1. The labels highlighted in green are the sections of the thermodynamic cycle with thermocouple measurement data. The process flow diagram provides detail on the flow path of the working fluid (air) within the ST-CHP power cycle. Air states are numbered before and after each component for reference purposes when presenting the mathematical model. Air is first pressurised in the compressor (C) and then the pressurised air passes into the cold side of the recuperator through a rubber hose. The cold side of the recuperator preheats the air before it is passed into the solar receiver. The receiver then heats the air further using solar radiation before it is passed into the combustion chamber. Liquid Petroleum Gas (LPG) is then used to heat the air in the combustion chamber (Comb) to the operation point of the turbine inlet before being expanded through the turbine (T). The exhaust heat from the turbine is then primarily recovered by passing the air through the recuperator. The subsequent low-temperature exhaust heat from the recuperator is captured by passing the air through a thermal energy storage unit before being released back into the atmosphere.

2.1. Solar tracker

The solar tracker comprising a dual-axis elevation-azimuth actuation system and steel support frame was designed by the University of Pretoria and constructed on the roof of Engineering Building 2 at the University of Pretoria, South Africa. A novel stow drive (linear actuator) allowed the dish to fold inwards towards the receiver arm to protect the reflector from winds and storms [42]. A second linear actuator actuated the setup in the elevation axis and allowed for a 0° to 90° elevation range of motion (0° elevation defines the tracker facing the horizon while 90° elevation defines the tracker facing vertically upward). A slew drive rotated the frame along the azimuth axis allowing for a full 360° range of motion relative to the north. A leap-frogging, fuzzy logic control system

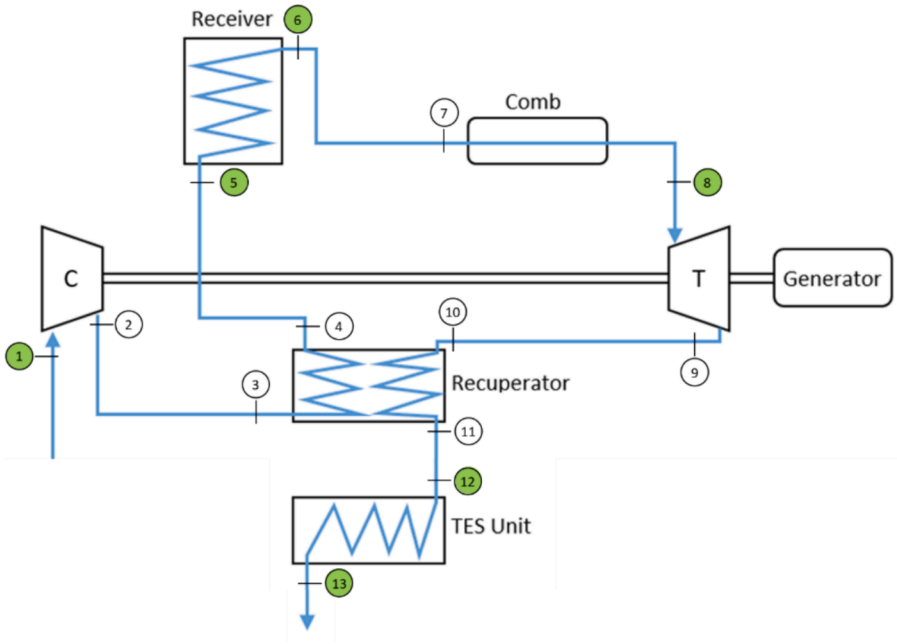

Fig. 1. ST-CHP prototype process flow diagram using air as the working fluid (green labels signify the points where process temperature was measured).

with rotary encoder feedback and NREL's Solar Position Algorithm provided automatic tracking of the sun throughout the test day with a tracking error of $< 0.5^{\circ}$ in both elevation and azimuth axes [43]. Fig. 2 presents the constructed collector at the test site.

2.2. Reflector

The reflector comprised a steel space frame onto which 46 elliptical reflector facets were mounted resulting in a 24.75 m^2 projected reflective area. The University of Pretoria developed the reflector facets [39–41]. The facets consisted of a sealed, concave base with an elliptical rim and a Sundog Solar Technology [44] polymer reflective membrane that was stretched and sealed over the elliptical rim of the base. When a vacuum is pulled in the space between the base and the membrane, the pressure causes the reflective membrane to take on a high specularity, elliptic paraboloid approximated shape that can concentrate sunlight into the solar receiver aperture.

2.3. Receiver

The coiled-tube open-cavity receiver was designed and manufactured at the University of Pretoria. The stainless-steel 316 receiver coil comprised just over 6 coil turns and had a square helical shape with an outer tube diameter of 88.9 mm and a tube thickness of 3 mm. 100-mm-thick ceramic fibre insulation was placed around the outer cavity. The receiver had a 39.5° wind skirt (formed by the insulation) with a 250 mm square aperture (see Fig. 3). Fig. 4 shows the insulated tubular cavity solar receiver with and without an aluminium cover.

Two types of thermocouples were used to capture the temperature readings within the solar receiver. The TC-40, type-K thermocouples were welded onto the surface of the receiver coil (see Fig. 5) and inserted into the coil at the inlet and outlet of the coil (recording the temperature of the air). The locations of the surface coil thermocouples welded onto the coil tube are illustrated in Fig. 5. Surface thermocouple 6 on the third coil turn was located on the inside of the receiver cavity (at the same coil length as surface thermocouple 5), while the rest of the receiver coil surface thermocouples were located on the outside of the receiver cavity (sandwiched between the coil tube and the cavity insulation). Surface thermocouple 6 was used to estimate the inner cavity temperature of the receiver.

The locations of inlet thermocouples are shown in Fig. 6, where the numbering system introduced '(2)' to each number to ensure that these

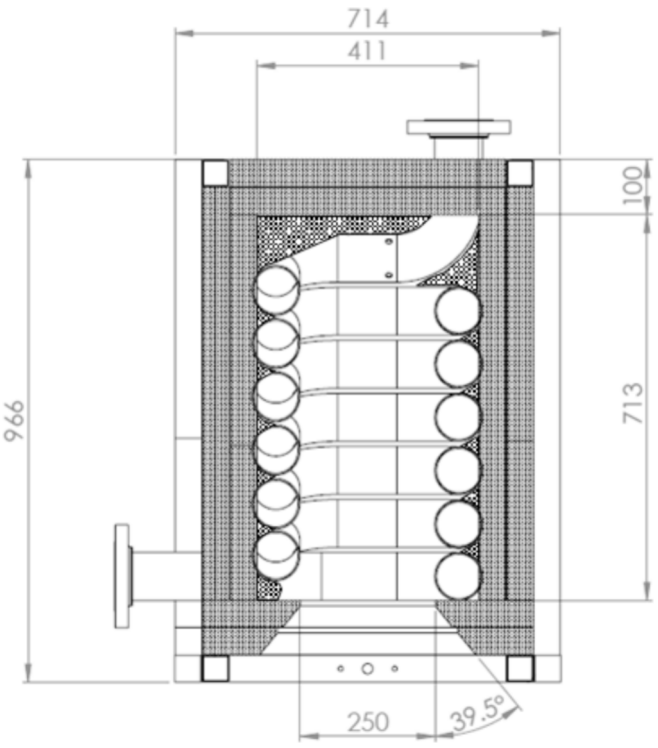

Fig. 3. Schematic drawing of receiver cavity (dimensions in mm).

thermocouple readings were not confused with the surface thermocouple readings. Thermocouples 2(2) to 5(2) were used to determine the average measured inlet air temperature and thermocouples 6(2) to 8(2) were used to determine the average measured outlet air temperature. Additionally, type-T thermocouples were placed at the outer surface of the insulation (5 mm into the insulation) which surrounded the receiver coil. These thermocouple types were directly in line with the coil surface thermocouples and were used to infer the outer insulation temperatures based on a 1-D conduction heat transfer assumption.

During the experimental procedure, receiver and ambient wind measurements were recorded to determine the heat losses from the solar receiver, whilst operating at elevated temperatures. Wind data were

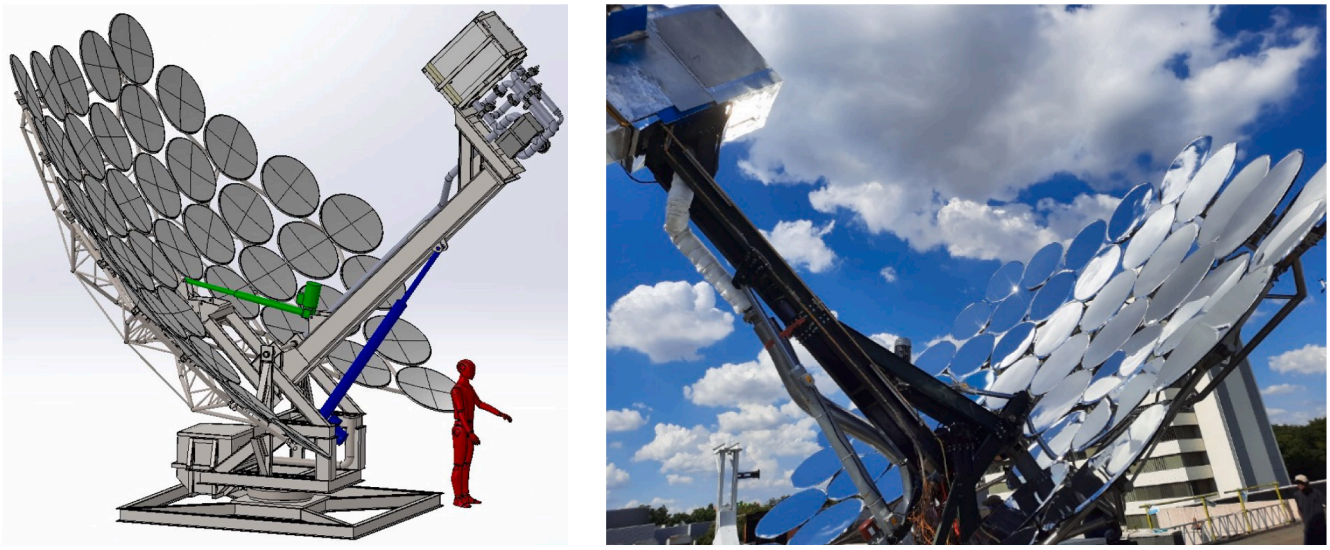

Fig. 2. ST-CHP solar collector (a) SolidWorks CAD assembly model, (b) prototype in operation.

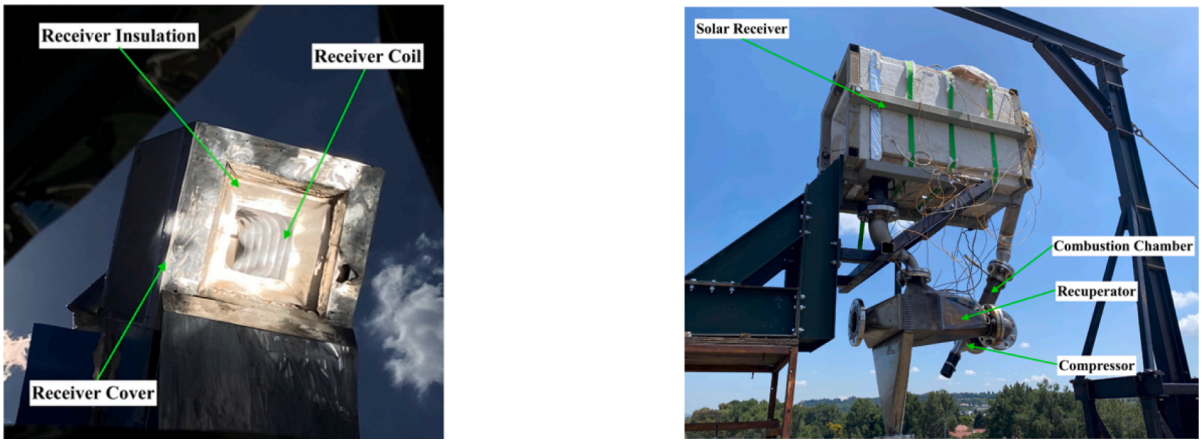

Fig. 4. Insulated tubular cavity solar receiver (a) in operation with cover and (b) during installation without cover.

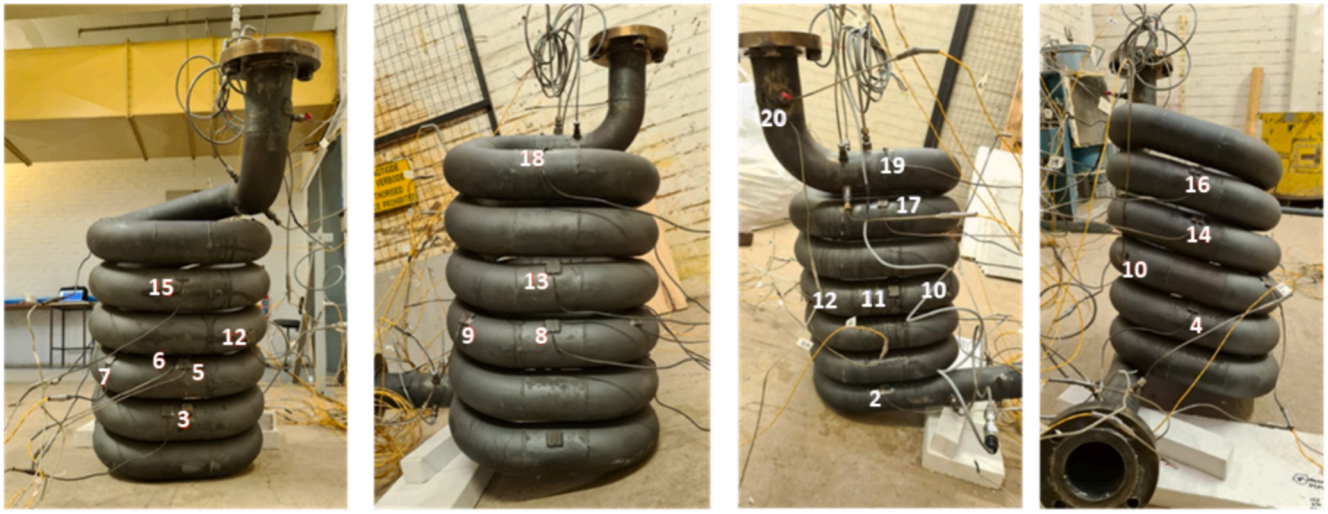

Fig. 5. Receiver coil surface-thermocouple locations (type-K).

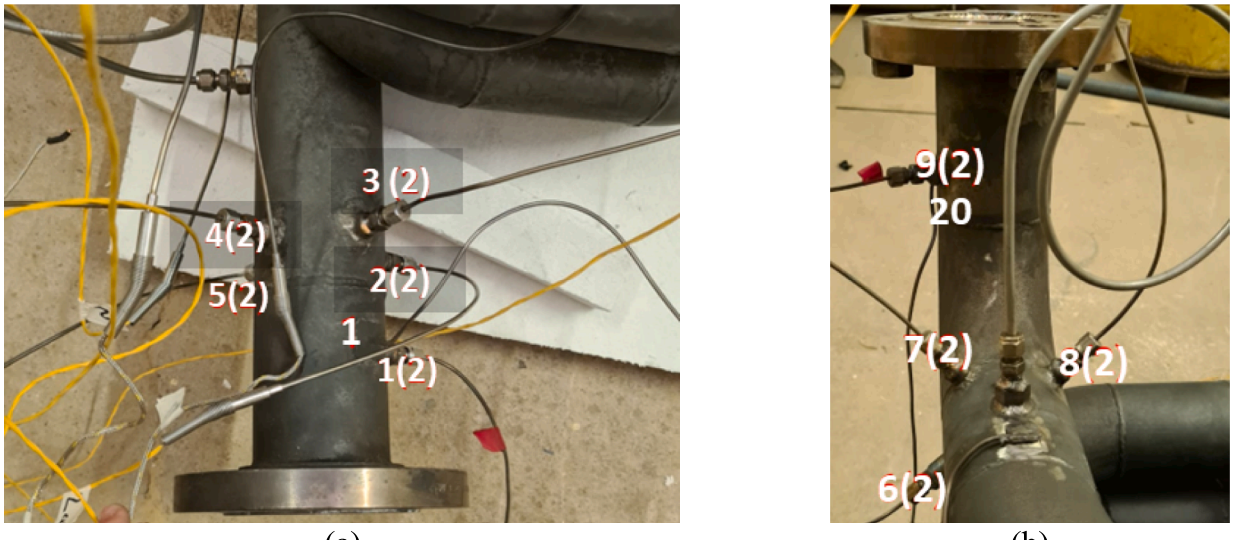

Fig. 6. Insertion thermocouple locations (a) at the receiver inlet using thermocouples '2(2)' to '5(2)' and (b) at the receiver outlet using thermocouples '6(2)' to '8(2)'.

captured 10 m from the test site using a Navis wireless wind speed and direction sensor and transferred to an anemometer wireless receiver [45]. The azimuth coordinates of the wind direction were given in terms of a wind vane coordinate system defining the direction that the wind was coming from (North = 0° or 360°, East = 90°, South = 180° and West = 270°). The schematic of the experimental layout and apparatus, used to capture the data, is represented in Fig. 7.

2.4. Micro gas turbine and combustion chamber

The micro gas turbine (see Fig. 8) was developed and manufactured by Samad Power [46]. Air bearings minimized friction of the rotor system and allowed the micro gas turbine to achieve the high rotational speeds required for efficient power generation at the given scale of the dish Brayton prototype. A custom power electronic unit designed and manufactured by Samad Power monitored and controlled the speed of the electrical motor/generator and diverted the generated electricity back to the grid. A LabView virtual interface coupled to the power electronics and DAQ unit formed the MGT control system which was used as the human–machine interface. The human–machine interface allowed for input/output control of the MGT speed, turbine inlet temperature, fuel flow rate and net power transfer to and from the MGT.

The combustion chamber was designed by Liu et al. [47] and manufactured by Samad Power. Combustion efficiencies were reported to reach up to 99 % using LPG and natural gas as fuel candidates [47]. A radial swirler promoted air–fuel mixing within the primary chamber before combustion. Jet holes provided diffusion of the air–fuel mixture into the secondary chamber which reduced flow speeds and promoted stable combustion. LPG was used as the combustion fuel. Four 48 kg gas canisters containing LPG at 10 bar were connected to the combustion chamber using a gas line spanning from the canisters located on the ground to the combustion chamber located at the end of the receiver arm. A Cole Parmer 32907–77 precision gas flow controller, interfacing with the control system, measured and controlled the LPG flow rate into the combustion chamber while an insertion thermocouple placed at the outlet of the combustion chamber measured the turbine inlet air temperature which allowed direct control of the micro gas turbine.

2.5. Recuperator

A counterflow, plate-style recuperator (see Table 3) was used to recuperate the exhaust air of the micro gas turbine. Fins of 0.2 mm thickness divided the high-temperature and cold-temperature channels into respective rectangular and triangular cross-section micro-channels. Fig. 9 presents the subassembly locations within the power-block of the ST-CHP dish-Brayton prototype.

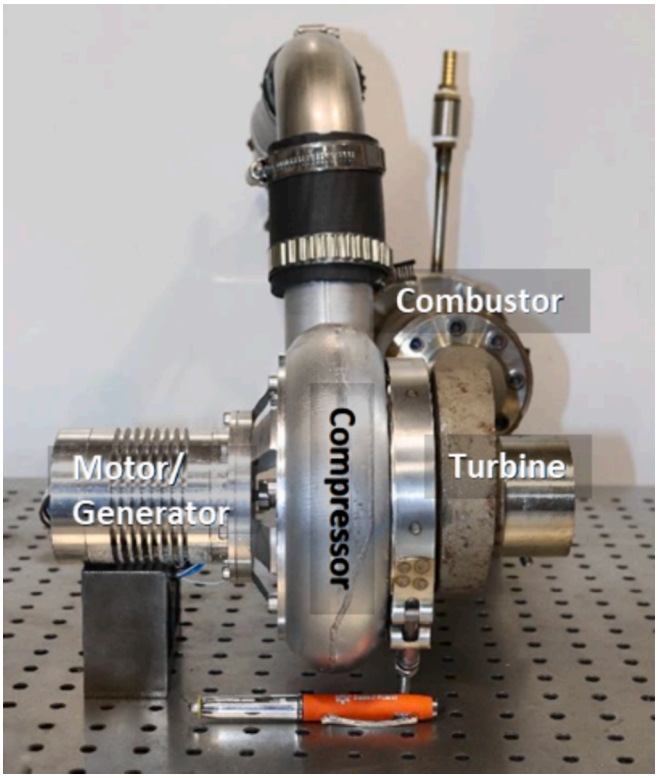

Fig. 8. ST-CHP micro gas turbine [46].

2.6. Thermal energy storage (TES)

A TES unit was fixed to the base of the solar collector and connected to the outlet of the turbine with the intent to capture the off-gas process

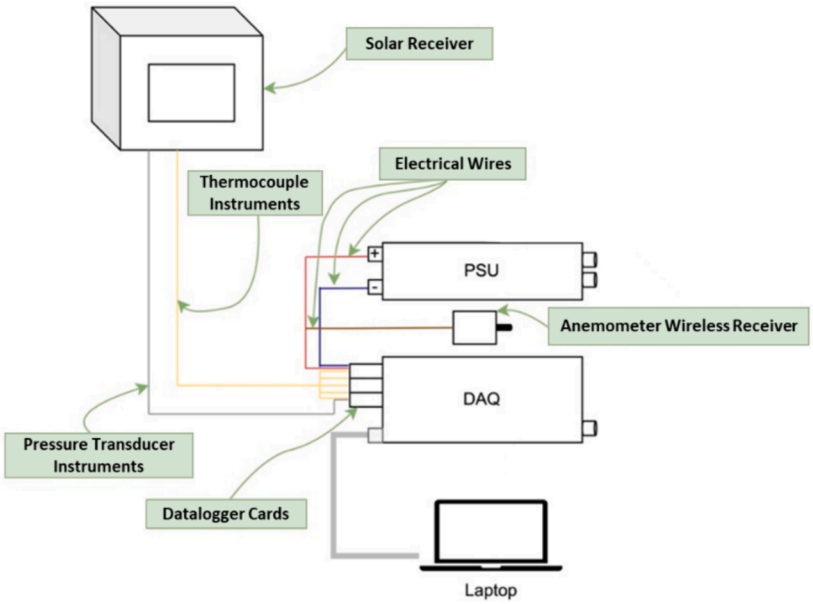

Fig. 7. Experimental layout and schematic for capturing wind data and receiver temperature data.

Table 3
Dimensional properties of the recuperator.

Description	High Pressure / Cold Side		Low Pressure / Hot Side
Number of channels (-)		58	56
Channel divider thickness (mm)		0.5	0.5
Channel height (mm)		2.85	4
Width (mm)		159	159
Fin division / micro channel shape		Triangular	Rectangular
Fin thickness (mm)		0.2	0.2
Micro channel dimensions	**Core**	**Divider**	
Length (mm)	100	80	180
Number of fins	20	52	100
Distance between each fin (mm)	15	6	1.38
Hydraulic diameter (mm)	2.81	2.65	2.05

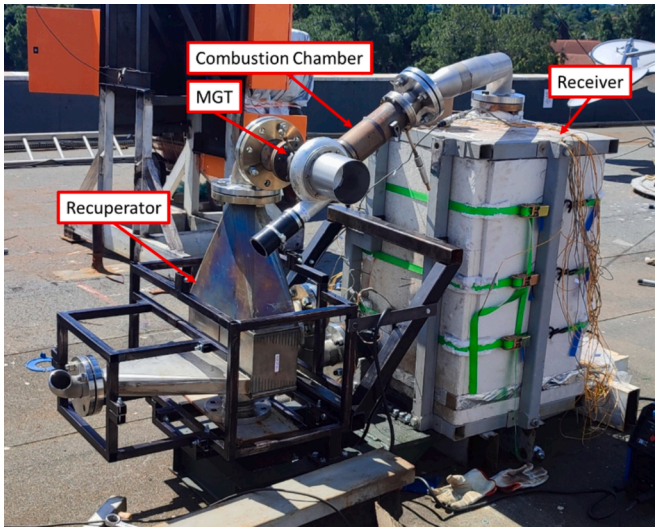

Fig. 9. Power-block of the dish-Brayton prototype containing the receiver, recuperator, combustion chamber and micro gas turbine.

heat. A phase-change solar salt medium was selected from an initial design study conducted by Humbert et al. [48]. 151 kg solar salt was stored in the TES unit with a stainless-steel coiled heat exchanger identical to the solar receiver coil. The solar salt had a theoretical melting temperature of 221.85 °C (495 K) and a 10 h charging time at a 550 K inlet air temperature (at a mass flow rate of 0.07 kg/s) to the TES unit [48]. Type-K thermocouples were welded along the coil length and additional thermocouples were placed into the bulk portion of the solar salt to measure bulk temperature.

2.7. Solar resource

The solar irradiance was measured and recorded by a SOLYS 2 weather station mounted 50 m from the testing location on the roof of Engineering Building 1 at the University of Pretoria. The roof of Engineering Building 1 is approximately eleven stories taller than the test site location. The solar data was actively captured for every minute of the day and was openly available to the public as part of the SAURAN initiative [49].

3. Methodology

A SimuPact numerical model as well as an analytical model were incorporated in the study to reduce interference (heat loss and pressure drop) from invasive telemetry, validate the numerical model, enrich the experimental data, and prompt follow-up parametric numerical studies for design optimization. The MGT was a prototype, with initial lab testing conducted in a non-hybridized configuration (simple cycle) to produce basic turbine and compressor maps at the manufacturer's facilities in the United Kingdom. The hybridization of the MGT with solar components as well as the addition of a recuperator meant that the MGT would be operating at an off-design condition compared to the turbine and compressor maps generated in the United Kingdom. Numerical supplementation benefited the analysis in predicting the MGT performance without requiring extra invasive telemetry at the MGT. Additionally, pressure drop values (per subassembly) were determined in a separate experiment at ambient temperature and then scaled to model the operational temperatures using a dimensional analysis (see Appendix A).

3.1. Numerical model

A model of the power plant was developed using SimuPact [50] simulation software to predict performance characteristics of the entire ST-CHP prototype. The numerical model allowed for an off-design performance prediction of the MGT since the MGT was operating at higher elevation, and with an added pressure drop than for which it was initially designed. Fundamental design information such as micro compressor and turbine performance and efficiency maps and solar receiver performance information comprised the initial model [51].

The combustor comprised a PID controller with heat and a small amount of air (representing LPG) added to the working fluid. The fuel added to the combustor was assumed to burn completely. A pressure drop through the combustor was modelled from ambient pressure test data (see Appendix A). The solar receiver was modelled by implementing a receiver-to-working fluid heat transfer coefficient and a receiver-to-ambient heat transfer coefficient. The heat transfer coefficients were adjusted to meet the outlet temperature measurements recorded during testing. The recuperator was simply modelled as a counter-flow heat exchanger, where the heat transfer coefficient between the cold and hot side was adjusted to fit design or experimental temperatures.

Constant boundary conditions were imposed to analyse steady-state conditions. The following boundary conditions were implemented:

- Measured ambient data
- Experimental temperature measurements
- Experimental MGT measurements (speed, fuel flow rate, electrical load, and estimated mechanical losses from designers)
- Solar heat input
- Analytical pressure drop values

The following assumptions were made:

- If analytical pressure drop values were not given, quadratic pressure loss for through-piping and valves was assumed, scaling for density changes with respect to the measured condition.
- Piping was assumed to be adiabatic, except for specific heat losses in the receiver and recuperator.
- Ambient temperature was assumed to be the same as compressor inlet temperature.
- The recuperator heat loss was estimated based on an overall heat transfer coefficient and the metal temperature of the recuperator versus the ambient temperature.

Using experimental steady-state measurements of temperatures, a working fluid mass flow rate (coinciding with analytical calculations) was iteratively determined by adjusting heat transfer coefficients, and fine-tuning MGT pressure ratios and efficiencies.

3.2. Analytical model

A mathematical model was developed to analyse the performance of

the thermodynamic cycle and to validate the numerical model.

3.2.1. Mass flow rate of air

The air mass flow rate, $\dot{m}_{air}$, was determined from the heat of combustion of the LPG combustion chamber presented in Equation 1. The lower heating value/net caloric value (*LHV*) for LPG was 45.8 MJ/kg and the density of LPG at 15 °C and 1 atm was 2.1 kg/m^3 [52]. The fuel volume flow rate, $\dot{V}_{f,slpm}$, was measured in standard litres per minute of propane gas by the Cole Parmer gas flow controller. Using the ideal gas law, the density of LPG was adjusted to the flow meter's STP conditions (25 °C and 1 atm) resulting in a value of $\rho_{f,STP} = 2.03$ kg/m^3. The discrepancy in viscosity between propane ($\mu_{pr,STP}$) and LPG ($\mu_{f,STP}$) was accounted for as shown in Equation 2. The viscosities of propane and LPG were determined to be 8.15×10^{-6} Pa.s and 7.84×10^{-6} Pa.s respectively, at STP conditions, using CoolProp [53].

$$\dot{m}_{air}(h_8 - h_7) + \dot{Q}_{loss,comb} = \dot{m}_f LHV \tag{1}$$

$$\dot{m}_f = \frac{\dot{V}_{f,slpm}}{1000 \times 60} \times \rho_{f,STP} \times \frac{\mu_{f,STP}}{\mu_{pr,STP}} \tag{2}$$

3.2.2. Receiver

The total solar potential incident on the solar collector was defined according to Equation 3. The total amount of concentrated solar energy that was intercepted by the receiver through the aperture was a function of the reflectivity of the reflector facets and the intercept factor of the solar collector as shown in Equation 4.

$$\dot{Q}_{sun} = I_{sun} A_{ref} \tag{3}$$

$$\dot{Q}_{int} = \bar{\rho}\gamma \dot{Q}_{sun} \tag{4}$$

The net heat gained by the receiver was a function of the intercepted solar radiation and the heat losses as shown in Equation 5, and was also determined experimentally from the enthalpy change at the receiver (see Equation 6 and see Fig. 1).

$$\dot{Q}_{net} = \dot{Q}_{int} - \dot{Q}_{cond} - \dot{Q}_{rad} - \dot{Q}_{conv} \tag{5}$$

$$\dot{Q}_{net} = \dot{m}_{air}(h_6 - h_5) \tag{6}$$

The thermal efficiency of the receiver was determined by taking the net heat gain of the receiver over the intercepted solar energy at the receiver as shown in Equation 7. The thermal efficiency of the solar collector was determined according to Equation 8.

$$\eta_{th,r} = \frac{\dot{Q}_{net}}{\dot{Q}_{int}} \tag{7}$$

$$\eta_{th,col} = \frac{\dot{Q}_{net}}{\dot{Q}_{sun}} \tag{8}$$

Receiver conduction heat transfer losses through the surrounding ceramic fibre insulation boards were determined using Equation 9. Temperatures on the walls of the inner cavity insulation were assumed to equate to the average outer-cavity (outer-coil) temperatures (per side). The average outer cavity temperatures were measured using the coil surface thermocouples in Fig. 5 which directly interfaced with the inner-cavity insulation. Temperatures on the outer-insulation faces were measured as mentioned in Section 2.3. Craig et al. [38] showed that the 100-mm-thick insulation in the corners had a minimal effect on the conduction heat losses. As a result, only the relevant cross-sectional area of the inner insulation faces (per side) where considered.

The inner insulation within the receiver cavity was 0.713 m high and 0.411 m wide. The lateral (front, back, left and right) walls of the inner insulation had a conductive area of $A_{front} = A_{back} = A_{left} = A_{right} = 0.293$ m^2, the top insulation wall had a conductive area of $A_{top} = 0.169$ m^2, while the bottom insulation wall located around the aperture had a conductive area of $A_{bottom} = 0.106$ m^2. The insulation board had a thickness of $t = 0.095$ m on all six walls respectively since the outer surface insulation thermocouples were placed 5 mm into the insulation boards. The thermal conductivity, k, was 0.067 W/m.K, 0.136 W/m.K, and 0.190 W/m.K at 400 °C, 800 °C, and 1200 °C respectively [54]. Equation 9 was used to determine the conduction heat losses through all six sides of the solar receiver.

$$\dot{Q}_{cond} = \sum_{\substack{i=front,back,\\ left,right,\\ top,bottom}} k_i A_i \frac{\left(T_{ins\ inner,i} - T_{ins\ outer,i}\right)}{t} \tag{9}$$

The radiation heat loss through the receiver aperture was determined using Equation 10 as suggested by Le Roux et al. [14]. A_{ap} was the aperture area which was determined to be 0.0625 m^2, and the effective emissivity (ε_{eff}) of the stainless-steel coil was calculated using the correlation developed by Jilte et al. [55]. The cavity emissivity was taken as for 316 stainless-steel oxidized at a temperature above 1100 K (0.69 at 400 K and 0.73 at 1000 K) [56,57], and the geometric surface area of the inner-cavity was 0.731 m^2.

$$\dot{Q}_{rad} = \sigma \varepsilon_{eff} A_{ap} \left(T^4_{cav\ inner} - T^4_{amb}\right) \tag{10}$$

Multiple factors play a role in the dynamics associated with the convection heat transfer mechanism from the receiver cavity, namely: ambient temperature, cavity temperature, cavity geometry, wind velocity, and wind incidence angle. Convection heat loss from the receiver was determined from the average natural convection of the correlations of Abbasi-Shavazi et al. [58] and Wu et al. [59], superimposed with the forced convection correlation of Ma [60] as it was found to predict the free-forced convection heat loss from the receiver with reasonable accuracy [61].

Surface thermocouple 5 and surface thermocouple 6 located on the third coil turn of the receiver were used to estimate the average inner cavity temperature. This was achieved by assuming that the temperature ratio between surface thermocouples 5 and 6 equated to the temperature ratio of average inner and outer cavity temperatures.

3.2.3. Micro gas turbine

The micro gas turbine and compressor maps were not modelled in the analytical study. To compare analytical results with the SimuPact model, the outlet temperature of the compressor was estimated in the analytical model as a function of MGT speed (in krpm) from MGT experimental data, captured by Samad Power in Equation 11.

$$T_2 = 1.2921\omega - 29.912 \tag{11}$$

3.2.4. Recuperator

The analysis of the recuperator was carried out to validate the recuperator effectiveness determined from state temperatures of the SimuPact model using the NTU-effectiveness method [62,63]. An initial iteration determined the recuperator effectiveness from the perspective of state temperatures followed by a second iteration based on the recuperator geometry (see Table 3). Cold side inlet and outlet temperatures were indirectly measured. An iterative approach was taken towards the hot side inlet and outlet state temperatures until convergence was reached in recuperator effectiveness. Further detail is provided in Appendix D.

3.2.5. Pressure drop

A dimensional analysis was performed to estimate pressure drop values during operating conditions. The pressure drop of each component was non-dimensionalised to a pressure coefficient term that was a function of the Reynolds number of the process air moving through the component. The pressure drop through each component was defined

according to Equation 12. Detail on the analysis and resulting pressure coefficient relations are given in Appendix A.

$$\Delta P = Cp \times \frac{\rho V^2}{2} \tag{12}$$

3.2.6. Heat loss from process piping

Heat loss from the connecting process pipes between subassemblies was analytically modelled as a series of conduction, convection, and radiation modes until it was dissipated into the ambient. A thermal resistance network was constructed for both the process pipe as well as the connecting flanges. Insulation blanket covered the process pipe but most of the flanges were left exposed to the ambient. A detailed heat loss model is presented in Appendix C.

3.3. Experimental procedure

Testing took place at the University of Pretoria, South Africa. Before the testing procedure was initiated, the facets were initially aligned using a laser pointer fixed to a self-levelling gyroscope while the dish faced vertically upwards (90° elevation angle). This method proved to be inaccurate, with large flux spillage at the receiver aperture being apparent during automatic tracking and resulted in a subsequent visual alignment of the facets being performed during the initial stages of automatic tracking while the dish faced the sun. Facet membrane depths were also set and refined during this initial period of visual inspection.

The tracker was initially in full-stow position, the power supply was off, and the dish was folded over on the receiver arm for protection. Power was switched on to the control system, solar tracker, and the micro gas turbine. The operator set a turbine speed on the HMI which caused the generator/motor to spin the turbine, pushing air through the process piping. The combustion chamber was ignited to provide the micro gas turbine with a 1200 K inlet temperature setpoint. The micro gas turbine speed was selected by the operator which determined the net power at the turbine. The dish folded open into an active tracking position and the solar tracker was moved to face the sun after which the active tracking sequence was initiated.

The active tracking sequence controlled the tracker to follow the sun as it moved across the sky and the solar radiation was concentrated into the receiver which heated up the receiver coils. The receiver coils eventually reached a positive temperature difference between the inner coil surface and the process air moving through the coils which resulted in a net heat gain in the solar receiver. The MGT operator selected a speed that promoted a net electrical output from the turbine, and steady state was attempted with periodic adjustment of the MGT speed and turbine inlet temperature. Sensor data were collected throughout the testing period.

4. Results

4.1. Transient test results

Full-scale on-sun testing of the ST-CHP experimental setup took place on the 30th of March 2022. The temperature sensor data and MGT sensor data that were captured during testing are presented as a function of time (see Fig. 10 and Fig. 11). An experimental log of the test period is presented in Table 4 detailing the ignition and tracking sequence, noting periods of cloud cover. Detail on the measurement and combined uncertainties of the test results is presented in Appendix B.

Fig. 10 presents the temperature sensor data during the test period. From the point of ignition of the combustion chamber at 13:50, it took approximately 22 min for active tracking to occur and 35 min for a net heat gain to occur from the receiver. Cloud cover interrupted the testing before steady state could be reached at 14:54 and flame out occurred between 15:10 and 16:26 due to technical difficulties. The combustion chamber was reignited at 16:26 and the solar receiver and MGT (excluding TES) reached steady-state temperature conditions within 19 min at 16:46. The MGT sensor data presented in Fig. 11 show how power was generated between 16:26 and 16:52. A maximum electrical power output of about 400 W was generated intermittently before the MGT reached a steady-state speed of 130 krpm at 16:36 to 16:50. During this time the outlet temperature from the receiver increased from 665 °C to a maximum of 696 °C, and the fuel mass flow rate reduced from 0.52 g/s to 0.43 g/s. MGT electrical power generation decreased from a value of between 215 W and 288 W to between 136 W and 155 W. It is important to note that the micro gas turbine was successfully operated at different elevation angles during the test period which was a concern given the prototype air bearing design.

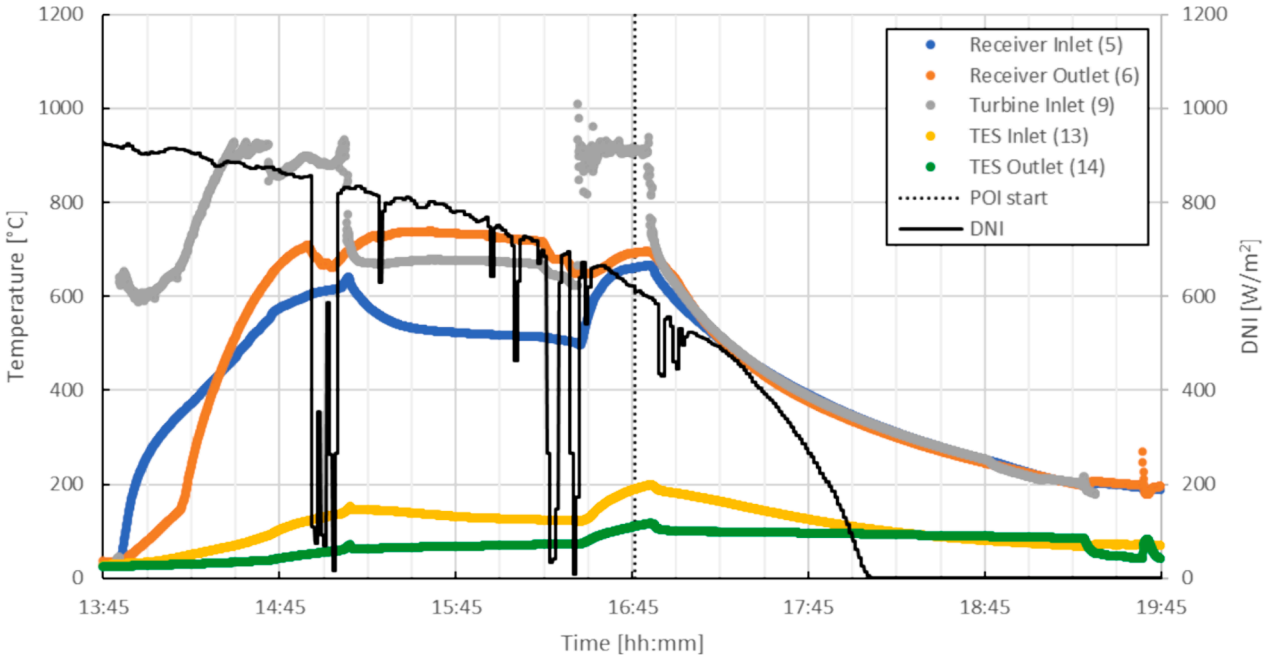

Fig. 10. Temperature sensor data for the testing conducted on 30 March 2022.

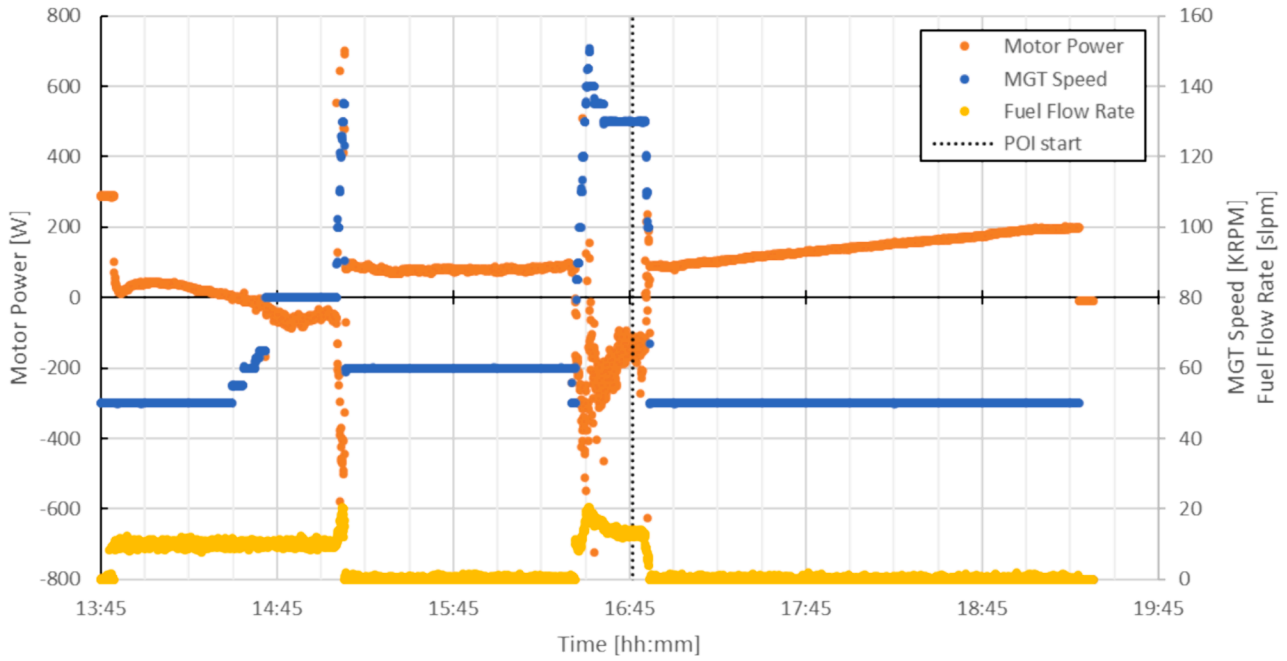

Fig. 11. MGT sensor data for testing conducted on 30 March 2022.

Table 4
Testing log from 30 March 2022.

Time Stamp	Comment
13:40	Start-up sequence initiated
13:50	Combustion chamber on
14:12	Active tracking sequence initiated
14:25	Net heat gain from the receiver
14:54	Cloud cover 1 started
15:03	Cloud cover 1 ended
15:10	Combustion chamber off
16:26	Combustion chamber on
16:45	Steady state temperature conditions reached
16:52	Shut down initiated
	• Tracker moved off sun • Combustion chamber off • Tracker placed in full-stow position
19:20	MGT off
19:39	MGT on
19:41	MGT off
19:45	Test end

4.2. Steady-state analysis

A steady-state period was defined between 16:46 and 16:48 during the testing on 30 March 2022 to characterise the performance of the solar thermal plant. The period was chosen for steady-state analysis as this period was characterised by the least amount of change in measurement data. It should be noted however that steady state could never truly be reached. Ambient conditions were constantly fluctuating, receiver inlet and outlet temperatures were still increasing slightly and insulation temperatures in the receiver were still increasing slightly. The effects of these dynamics are however assumed to be negligible. A summary of the steady-state ambient conditions is given in Table 5. Due to the time of day at which the point of interest was selected, the direct normal irradiance was relatively low, but an appropriate analysis could still be conducted. The variation column defines the minimum and maximum variation around the mean value provided in the measured value column.

The simulation mass flow rate and temperature results are compared with the measured values for the point of interest in Table 6. MGT,

Table 5
Measured ambient data and tracking data for point of interest at 16:46 – 16:48 (30 March 2022).

Description	Measured Value	Variation
Ambient Data		
Ambient temperature (K)	297.91	+0.03/-0.03
Ambient pressure (kPa)	86.21	+0.004/-0.004
Ambient wind speed (m/s)	1.13	+0.97/-0.50
Wind vane direction (degrees from North)	22.45	+79.08/-131.93
Direct normal irradiance (W/m^2)	610.85	+0.75/-0.75
Tracker Orientation		
Elevation angle (degrees)	17.49	+0.10/-0.11
Azimuth angle (degrees from North)	283.36	+0.06/-0.07

receiver, recuperator, and combustion chamber performance are summarized in Table 7. The simulation model meets all the target temperature values of the experimentally-measured data within 1 % error (except for the TES inlet and outlet temperatures). When comparing the numerical simulation to the analytical model, the system pressures are comparable within 3.5 % difference, the compressor outlet pressure deviates by 2.3 % and the turbine outlet pressure deviates by 0.6 %. From the simulation results it may be observed that the dominating pressure drop is found in the combustion chamber and in the recuperator cold side (besides the pressure drop over the turbine). The pressure drop values from the SimuPact model varied slightly from the analytical values since the simulation model incorporated quadratic extrapolation on an earlier set of analytical pressure drop values and no pressure drop was assumed in the connecting process piping. The numerical model focused on modelling the entire plant above the TES unit so there was a discrepancy regarding the inlet and outlet process temperatures to the TES unit between the numerical model results and the experimental results. The air mass flow rate determined by the SimuPact numerical model was found to meet the target air mass flow rate determined by the analytical model summarized in Table 6. A detailed analysis of the recuperator is presented in Appendix C.

The SimuPact numerical model results show that the dish-Brayton plant was able to produce 144.46 W of electricity and 19.24 kW of process heat from a net heat input of 2.53 kW from the receiver and 17.99 kW from the combustion chamber during the two-minute steady-

Table 6
SimuPact simulation results for point of interest at 16:46 – 16:48 (30 March 2022).

Description	Experimental Results	SimuPact Simulation	Analytical Model
Mass flow rates			
Fuel flow rate (slpm)	13.10	–	13.10*
Air mass flow rate (g/s)	–	72.8**	72.2
Temperatures and Pressures			
Compressor inlet temperature, T_1 (K)	298	298*	298*
Compressor inlet pressure, P_1 (kPa)	86.21	86.20*	86.21*
Compressor outlet temperature, T_2 (K)	–	409	411
Compressor outlet pressure, P_2 (kPa)	–	195.93	200.45
Recuperator (cold) inlet temperature, T_3 (K)	–	409	408
Recuperator (cold) outlet temperature, T_4 (K)	–	935	940
Receiver inlet temperature, T_5 (K)	935	935*	935*
Receiver outlet temperature, T_6 (K)	966	966*	966*
Combustion chamber inlet temperature, T_7 (K)	–	966	959
Turbine inlet temperature, T_8 (K)	1184	1184*	1184*
Turbine inlet pressure, P_8 (kPa)	–	174.56	175.35
Turbine outlet temperature, T_9 (K)	–	1068	1072
Turbine outlet pressure, P_9 (kPa)	–	90.31	90.85
Recuperator (hot) inlet temperature, T_{10} (K)	–	1068	1072
Recuperator (hot) outlet temperature, T_{11} (K)	–	555	556
TES inlet temperature, T_{12} (K)	465	555	465*
TES outlet temperature, T_{13} (K)	385	337	385*
TES outlet pressure, P_{13} (K)	86.21	86.20*	86.21*
Pressure drop			
Recuperator (cold) pressure drop, $dP_{3\text{-}4}$ (kPa)	–	5.52**	4.51
Receiver pressure drop, $dP_{5\text{-}6}$ (kPa)	–	1.33**	1.09
Combustion chamber pressure drop, $dP_{7\text{-}8}$ (kPa)	–	13.43**	15.23
Recuperator (hot) pressure drop, $dP_{10\text{-}11}$ (kPa)	–	1.87**	1.91

* Experimental result used as input or target value
** Analytical model used as input or target value

Table 7
Summary of receiver, combustion chamber, MGT, and recuperator performance for point of interest at 16:46 – 16:48 (30 March 2022).

Description	Experimental Results	SimuPact Simulation	Analytical Model
Solar receiver			
Available solar energy (kW)	15.06	–	15.06*
Net heat captured in receiver (kW)	2.54	2.53*	2.54*
Micro-gas turbine			
Heat of combustion (kW)	19.49	–	19.49*
Net heat of combustion (kW)	–	17.99**	18.68
MGT speed (krpm)	130	130*	130*
Compressor pressure ratio (-)	–	2.27	2.33
Compressor work (kW)	–	8.17	–
Compressor efficiency (-)	–	0.71	–
Turbine expansion ratio (-)	–	1.93	1.93***
Turbine work (kW)	–	8.64	–
Turbine efficiency (-)	–	0.57	–
MGT mechanical loss (W)	–	319.2	–
MGT mechanical shaft work (W)	–	157.07	–
MGT electrical output (W)	144.46	144.50*	–
Recuperator			
Effectiveness (-)	–	0.80	0.80
Heat recuperated (kW)	–	40.91	41.12
Heat of off-gas (kW)	–	19.24	18.98
Thermal energy storage unit (TES)			
Heat captured by TES (kW)	5.94	–	–

* Experimental result used as input or target value
** Analytical model used as input or target value
*** SimuPact model used as input or target value

Table 8
Air mass flow rate calculation for point of interest at 16:46 – 16:48 (30 March 2022).

Description	Analytical Model
Density of LPG @ STP (kg/m^3)	2.03
LHV of LPG (kJ/m^3) [52]	92,954
Propane to LPG viscosity correction factor	0.96
Fuel flow rate (kg/s)	4.26E-04
Heat loss from combustion chamber (kW)	0.81
Enthalpy before combustion chamber (kJ/kg)	1126
Enthalpy after combustion chamber (kJ/kg)	1385
Air mass flow rate (kg/s)	0.0722

state period. Based on an analytical enthalpy change between the TES inlet and TES outlet, 5.94 kW (31 %) of the 19.24 kW off-gassed process heat was captured. Based on the enthalpy change between the recuperator hot side outlet (state 11) and the TES inlet (state 12), it is estimated that approximately 7 kW of process heat was lost from the process piping before entering the TES unit. This is more than the heat that was captured by the TES unit. More stringent insulation techniques along the connecting process piping are advised for future work to mitigate this heat loss to the ambient.

4.2.1. Combustion chamber

Equation 1 and Equation 2 were used to analytically determine the air mass flow rate from the fuel flow rate measurement and the enthalpy change through the combustion chamber (see Table 8). The SimuPact numerical model determined the air mass flow rate primarily through modelling and analysing the micro gas turbine, based on design performance curves (pressure ratio and efficiency versus corrected mass flow supplied by Samad Power [46]). An iterative approach between simulation and analytical methods was conducted until close agreement was achieved within 1 % difference (see Table 6). Obtaining an agreement of the air mass flow rate values was a fundamental principal from which the rest of the numerical and analytical study was conducted. Based on the analytical results, the net heat gain of the combustion chamber was 18.68 kW from an available 19.49 kW suggesting a thermal efficiency of 96 %.

Heat loss was analytically determined for the process connection between the receiver outlet and the combustion chamber inlet. A value of 0.58 kW was determined, reducing the air temperature of 966 K from the receiver outlet to 959 K at the combustion chamber inlet. A pipe length of 1 m with an inner diameter of 83 mm, a pipe thickness of 3 mm and an insulation thickness of 100 mm was used as inputs to the heat loss model. The majority of the heat loss occurred at the exposed flange connections. A second conservative heat loss of 0.81 kW was analytically determined to occur from the combustion chamber itself by considering the average surface temperature of the outside of the combustion chamber to be 1566 K. This value was estimated by determining the average between the inlet air temperature to the combustion chamber (959 K) and the maximum flame temperature of the combustion fuel (2173 K [52]). The length of the combustion chamber was 300 mm and had an outer diameter of 87 mm and an insulation thickness of 50 mm. Enthalpy values before and after the combustion chamber were determined from temperature values using CoolProp [53].

4.2.2. Collector and receiver

The average coil surface temperature is plotted in Fig. 12 as a function of coil length with inlet and outlet air temperatures. Surface thermocouple 6 located on the inner surface of the receiver coil

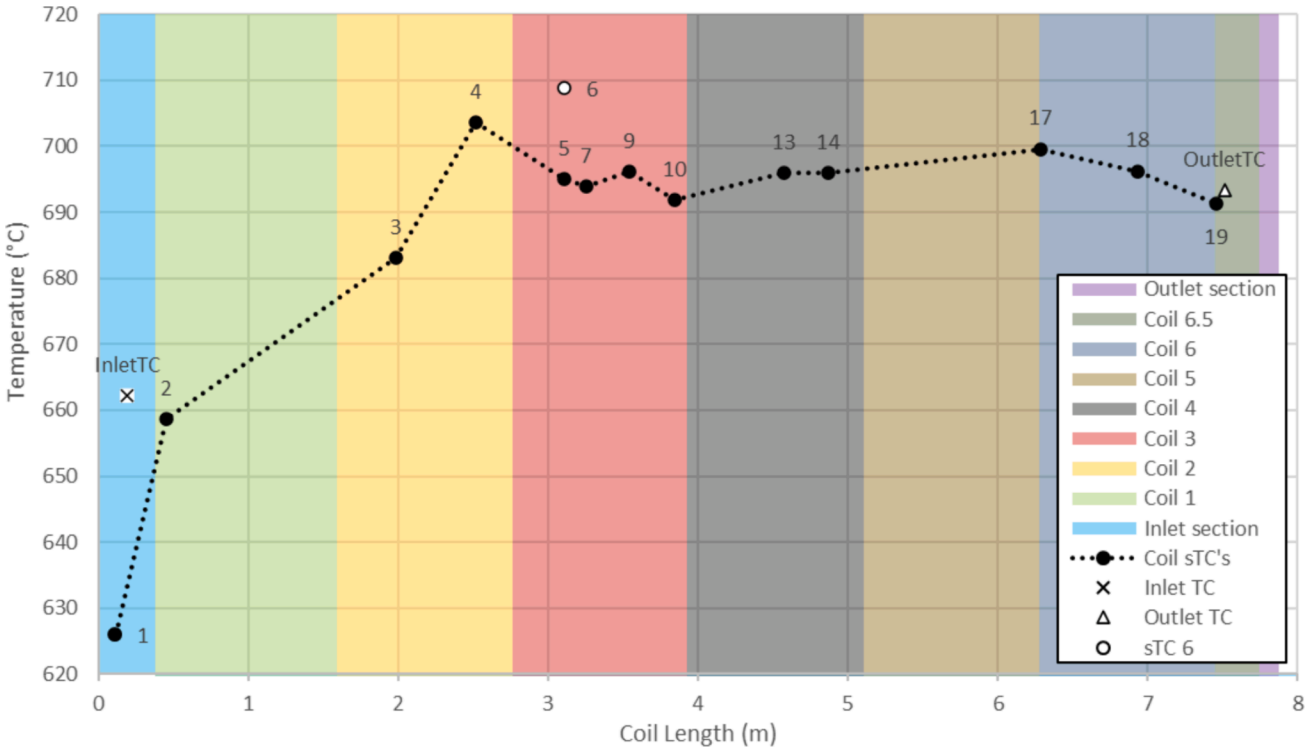

Fig. 12. Average coil surface temperature with inlet and outlet process air temperatures as a function of coil length for point of interest at 16:46 – 16:48 (30 March 2022).

measured a surface temperature 2 % higher (in degrees Celsius) than that of surface thermocouple 5 located on the outside of the receiver coil. The average inner-cavity surface temperature of the receiver was estimated by multiplying the average outer-cavity surface temperature by 1.02 (in degrees Celsius). The overall performance of the solar receiver was evaluated in terms of the net rate of heat gain, heat loss (conduction, radiation, and convection), available solar energy, intercept factor, and the receiver's solar and thermal efficiency. These results have been summarised in Table 9 for the steady-state point of interest.

The distribution of heat loss from the receiver, on average, was 10 %, 51 % and 39 % in terms of conduction, convection, and radiation heat loss, respectively. The conduction heat loss rate experienced during this steady-state point of interest was relatively low, illustrating the effectiveness of the ceramic insulation boards surrounding the solar receiver. The solar receiver was positioned at an elevation angle of between 17.4° – 17.6° which is expected to result in an elevated convection heat loss according to the study performed by Craig et al. [38] and Swanepoel et al. [61]. The total heat losses in the receiver were estimated to be 6.10 kW. The intercept factor was found to be 64 % owing to the spillage at the receiver from inadequate aiming and calibration of the parabolic reflective facets. The membrane depth also varied as a function of ambient conditions [64]. The intercept factor can be improved by implementing more stringent aiming and reflector calibration practices such as moonlight calibration using lunar flux mapping [39,41]. Alternative options for improving reflector facet optical performance would be to consider active membrane depth control or solid facet options [65–67]. The solar receiver was found to have a thermal efficiency of 29 % as well as a collector efficiency of 17 %. The receiver thermal efficiency was low during this steady-state point of interest due to the low availability of solar DNI present due to the time of day when the sun was setting and the low elevation angle.

Table 9
Summary of receiver performance for point of interest at 16:46 – 16:48 (30 March 2022).

Description	Experimental Results	SimuPact Simulation	Analytical Model
Direct normal irradiance (W/m^2)	610.85	–	610.85*
Average receiver outer-cavity temperature (K)	965	–	965*
Average receiver inner-cavity temperature (K)	979	–	979*
Available solar energy (kW)	15.06	–	15.06*
Solar energy reflected (kW)	–	–	13.55
Net receiver heat captured (kW)	2.54	2.53*	2.54*
Receiver conduction heat loss (kW)	0.61	–	0.61*
Receiver radiation heat loss (kW)	3.12	–	3.12*
Receiver convection heat loss (kW)	–	–	2.37
Total receiver heat loss (kW)	–	–	6.10
Collector intercept factor (-)	–	–	0.64
Receiver thermal efficiency (-)	–	–	0.29
Collector thermal efficiency (-)	–	–	0.17

* Experimental result used as input or target value

5. Discussion

5.1. Potential performance of the receiver

Since a steady-state period of interest was only able to be captured in the late afternoon, the performance of the receiver and collector were subsequently low. To provide more detail on the holistic performance of the receiver, average conditions for a full day of operation and conditions at peak operation were analysed. To estimate the potential performance of the solar receiver and collector for the day of 30 March 2022, two case studies were considered using an analytical approach: the average operating conditions case (06:00 – 18:00) and the peak operating conditions case (11:00 – 14:00).

The following assumptions were made:

- The heat transfer coefficient for the captured heat between the receiver coil and the process air was determined for the steady-state point of interest in Section 4.2 (using Equation 13), and was assumed

to be constant for both operating conditions. This is a major simplification made for the purposes of making a crude estimation of the performance impact on the receiver.

- The inlet process air temperature and mass flow rate to the receiver was assumed to be constant at the conditions measured in Section 4.2 (935 K and 0.072 kg/s respectively). The combustion chamber, MGT and recuperator operating conditions were, therefore, assumed to be constant.
- The process air pressure was assumed to be constant at 1 bar for simplicity.
- Conduction, convection, and radiation heat loss was determined based on Section 3.2.2. The outer insulation temperature was assumed constant, and the ambient temperature was averaged over the period considered in the case.
- The intercept factor for the collector was assumed constant at an average value of 0.64, based on the value determined in Section 4.2.

$$\widehat{h}_{air} = \frac{\dot{Q}_{net}}{A_{coil}\left(T_{cav\,inner} - T_{b,air}\right)} \tag{13}$$

Table 10 summarizes the receiver and collector performance predictions for both average and peak performance scenarios considered. The average collector elevation angle was determined to be 35° and 56.04° for the average operating conditions and peak operating conditions, respectively. The average available solar energy increased by 17 % and 54 % respectively, leading to an increase in the receiver average inner-cavity temperature of between 4 % and 9 % (in Kelvin), respectively. Due to the elevation angle increasing and despite the increased inner-cavity temperature, the average total heat loss from the receiver cavity changed by −1 % and +1 % for the average and peak operating conditions, respectively. From this analysis, the average receiver thermal efficiency is expected to be 40 % and the average collector efficiency is 23 % for the average operation operating conditions case, producing a net captured heat of 4.10 kW on average (a 61 % improvement in net heat captured, compared to the experimental steady-state point of interest). For the peak performance case, the average receiver thermal efficiency was determined to be 53 % and the average collector efficiency was 31 %, producing a net captured heat of 7.10 kW (a 179 % improvement in net heat captured, compared to the experimental steady-state point of interest).

Table 10
Predicted performance of the solar receiver for 30 March 2022.

Description	Analytical Model	Average Conditions	Peak Conditions
Conditional parameters			
Time	16:46–16:48	6:00–18.00	10:00–14:00
Ambient temperature (K)	298	296	297
Solar DNI (W/m^2)	610.85	716.92	939.10
Elevation angle (degrees)	17.49	34.93	56.04
Collector performance			
Intercept factor (-)	0.64	0.64	0.64
Available solar energy (kW)	15.06*	17.67	23.15
Solar energy reflected (kW)	13.55	15.91	20.83
Average receiver inner-cavity temperature (K)	979*	1005	1056
Average receiver outer-cavity temperature (K)	965*	991	1041
Receiver conduction heat loss (kW)	0.61*	0.66	0.75
Receiver radiation heat loss (kW)	3.12*	3.48	4.25
Receiver convection heat loss (kW)	2.37	1.91	1.19
Total receiver heat loss (kW)	6.10	6.04	6.18
Net receiver heat captured (kW)	2.54*	4.10	7.10
Receiver thermal efficiency (-)	0.29	0.40	0.53
Collector thermal efficiency (-)	0.17	0.23	0.31

* Experimental result used as input or target value

The predicted performance of the receiver compares well with the previous successful field test carried out by Sanders Associates & Garret AiResearch in the 1980's [20–22] which obtained a receiver efficiency of 57 % and a collector efficiency of 48 %. The collector thermal efficiency did not compare well due to the low intercept factor determined in the current study. The performance improvement predicted for the receiver in the above case studies does not necessarily mean that there will be an improved performance of the entire ST-CHP prototype. The increase in process temperature at the outlet of the receiver is expected to affect the pressure drop at the subsequent process connections, specifically before the turbine, which would affect the MGT performance, and this would affect the operating conditions in the rest of the power cycle. A better approach to this analysis, would be to analyse the impact of the case studies on the performance of the entire prototype, which is recommended for future work.

From the thermodynamic perspective of process heat generation, fuel savings (see Equation 14) becomes an important parameter. The ST-CHP prototype allowed for a predicted fuel savings of between 12 % at experimental conditions and 33 % at peak operating conditions compared to fuel-only operation. Peak operation fuel savings may be further increased to an estimated 52 % if the intercept factor could be improved from the experimentally determined 64 %, to the design target of 90 %.

$$fuel\,savings = \frac{\dot{Q}_{net}}{\dot{Q}_{net} + \dot{m}_f LHV} \tag{14}$$

5.2. Pressure drop breakdown

It is evident that the added pressure drop from the auxiliary components (such as the receiver, recuperator, and connective piping) negatively impacted the performance of the micro gas turbine. When considering the analytical percentage pressure drop for each component in the cycle during the steady-state point of interest (relative to inlet pressure) it becomes clear that certain components have more of an impact compared to others, as indicated in Table 11. On the high-pressure side between the compressor and the turbine, the combustion chamber can be shown to have the largest pressure drop of 8 % (15.2 kPa), the pressure drop through the recuperator cold side and through the pipe connection between the receiver and combustion chamber then follow with both pressure drop values being 2.2 % (4.5 kPa and 4.3 kPa respectively). The pressure drop of the combustion chamber in a simple cycle (no solar hybridization, non-recuperated, see Fig. 13) is roughly 3 % according to Samad Power. The higher combustion chamber pressure drop in the ST-CHP prototype is mainly related to higher inlet air temperature (~950 K) to the combustion chamber compared to a simple cycle (~410 K). The pressure drop through the process pipe connecting the receiver to the combustion chamber is believed to be primarily due to the 3 inch to 2 inch reduction nozzle at the end of the pipe, which allowed for a direct flange connection to the combustion chamber. The added pressure drop from the solar receiver is only 0.6 % which barely

Table 11
Breakdown of pressure drop values in the ST-CHP prototype for the point of interest 16:46 – 16:48 (30 March 2022).

Component	Inlet pressure (kPa)	Pressure drop (-)
Recuperator cold side (3–4)	200.5	2.2 %
Solar receiver (5–6)	196.0	0.6 %
Pipe between receiver to combustion chamber (6–7)	195.0	2.2 %
Combustion chamber (7–8)	190.6	8.0 %
Recuperator hot side (10–11)	90.9	2.1 %
Piping to TES (11–12)	88.9	2.9 %
TES (12–13)	86.3	0.2 %

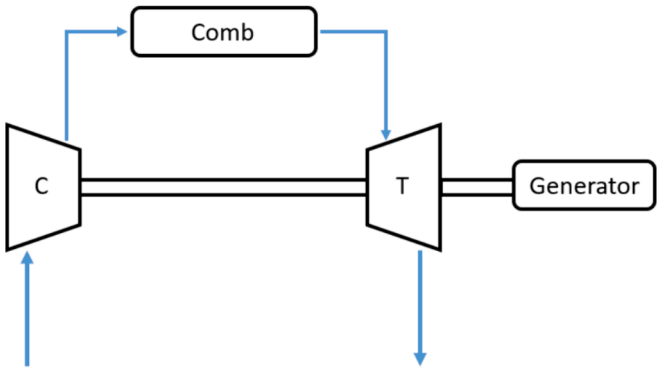

Fig. 13. MGT simple cycle flow diagram.

compares to that of the previously mentioned components. It is also important to note the 2.9 % (2.6 kPa) pressure drop through the process 3-inch piping connecting the recuperator hot outlet to the TES inlet. Much of this pressure drop occurs through the valve located at the inlet of the TES unit (1.1 kPa). The added pressure drop from the components after the turbine outlet would negatively impact the MGT performance as well. Reducing the length of pipe used or increasing the diameter in this connection and incorporating more pressure-friendly valves would improve performance.

To improve the performance of the micro gas turbine in the solar hybrid configuration, the hybridized sub-assemblies must be optimized against this pressure loss. Optimizing recuperators to minimize pressure loss while maintain recuperation effectiveness at the given recuperator size is challenging. The obvious solution would be to increase micro-channel and channel dimensions while maintaining heat transfer surface area which would increase the overall recuperator dimensions.

When considering the reduction nozzle in the process piping, the reduction nozzle was only required due to the reduced inlet diameter of the combustion chamber. It is recommended that the combustion chamber design be modified to decrease pressure drop by mitigating the reduction nozzle at the inlet of the combustion chamber as well as a holistic dimensional optimisation to decrease pressure drop in the combustion chamber itself. Reducing the combustion chamber pressure drop is a challenge that may require an active geometry control to allow for a successful cold start (ignition) and to continuously operate at steady state. Additionally, mitigating the pressure drop through the combustion chamber is often challenging since the pressure drop is required for adequate mixing of the fuel and air to enhance combustion and reduce emissions.

5.3. Potential MGT performance

The micro gas turbine was configured in a simple Brayton cycle for a secondary set of testing on the 31st of March 2022. This was done to confirm power generating potential without the effects of pressure drop from auxiliary units such as the receiver, recuperator, downstream piping and TES unit. A flow diagram is presented in Fig. 13. The test results are presented in Fig. 14.

A maximum steady-state power generation was found between 15:21:15 and 15:21:45, with a value of 1050 W at a MGT speed of 137 krpm and a fuel flow rate of 40 slpm. This is an increase in electrical output of 627 % with an estimated decrease in pressure drop of 39 % based on the current steady state data in Section 4.2. When observing the power generation at 130 krpm between 15:20:01 and 15:20:48, the power generation was within a range of 870 W and 989 W at a fuel flow rate of between 35.8 slpm and 37 slpm. Compared to the steady-state point in Table 6 and Table 7, this is an increase of between 502 % and 585 % in electrical power generation. The fuel consumption, however, also increases by between 173 % and 182 % for the simple cycle.

The power generation normalised by the fuel flow rate allows for the determination of whether the auxiliary components are in fact benefitting the electrical generation. On average the simple cycle produces a value of 0.026 kWe/slpm while the ST-CHP prototype produced a value of 0.011 kWe/slpm showing that the ST-CHP prototype was not beneficial in terms of electrical production from the plant at the current point of interest that was analysed. When considering the predicted average operating performance and the peak operating performance of the ST-CHP collector presented in Section 5.1, the normalised electrical production from the ST-CHP prototype increases to 0.012 kWe/slpm and 0.015 kWe/slpm, respectively. It is evident that the performance of the micro gas turbine (electrical output) is negatively impacted by the pressure drop of the hybridizing components (the receiver, recuperator, TES unit and connective process piping) and the combustion chamber operating at a higher inlet temperature. No information regarding the recuperated Brayton cycle performance (without solar hybridization) is available, therefore the effect of the pressure drop through the

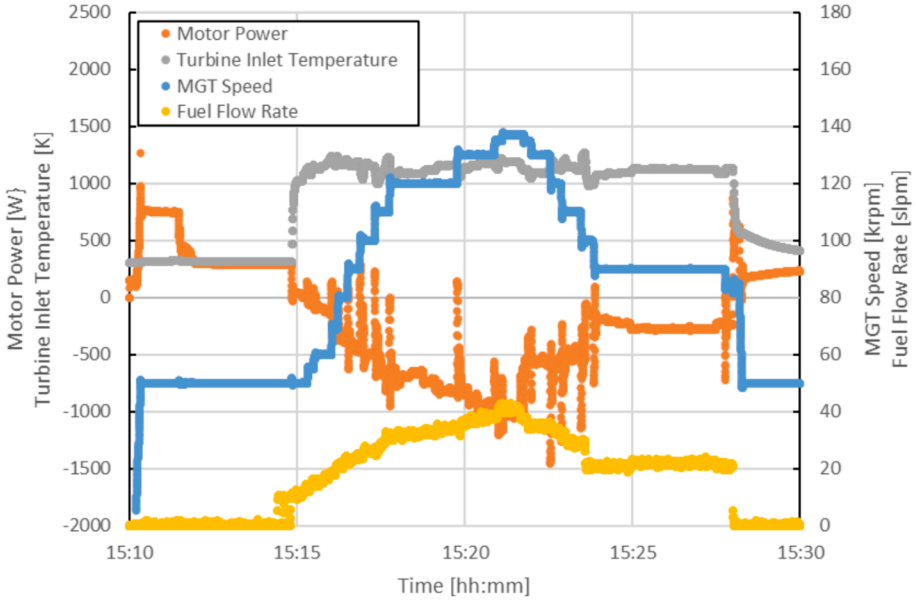

Fig. 14. MGT simple cycle test measurements for 31 March 2022.

recuperator is also considered to negatively impact performance.

5.4. Prospects

The ST-CHP plant is a prototype and there is significant room for improvement in both performance and manufacturing cost. The performance of the ST-CHP prototype may be characterised and compared with solar PV in terms of an energy utilisation factor (EUF). Commercially available solar PV units operate with a single electrical output at an EUF of between 15 % and 20 % during daytime operation [68,69]. Since the ST-CHP prototype has a CHP output from a solar and combustion fuel source, the EUF may be determined using Equation 15. The ST-CHP prototype has an EUF of between 17 % at the experimental steady state, and 16 % at estimated peak operating conditions (assuming outputs remain constant, and the solar input affects the required combustion heat input). The EUF of the ST-CHP prototype has a large potential for improvement [70]. An improvement of the intercept factor from the experimentally determined 64 % to the design point of 90 % (see Ref. [40]) would improve the EUF at peak operating conditions from 16 % to 18 %. The use of a combustion chamber in the ST-CHP prototype also allows for 24 h operation which provides a competitive edge over solar PV.

$$EUF = \frac{\dot{E}_{output} + \dot{Q}_{TES}}{\dot{Q}_{sun} + \dot{m}_f LHV} \tag{15}$$

6. Conclusion and recommendations

Initial on-sun solar tests were conducted on the Solar Turbo Combined Heat and Power prototype to serve as a proof of concept for power generation during field operation and identify improvements for future work. Solar hybridization of a novel recuperated micro gas turbine Brayton power cycle was investigated to determine the potential of solar preheating to reduce or replace consumption of combustion fuel to generate a combined heat and power output. The Solar Turbo Combined Heat and Power prototype with preheating from a faceted dish solar collector was tested during on-sun conditions. Liquified petroleum gas was used as the combustion fuel to reach inlet condition for the micro gas turbine. A self-sustained electrical power output was successfully generated ranging between 0.4 kWe and 0.1 kWe at a fuel flow rate between 20 slpm and 10 slpm while the solar direct normal irradiance was decreasing from 855 W/m^2 to 611 W/m^2.

A steady-state point of interest was identified and analysed to characterise the performance of the Solar Turbo Combined Heat and Power prototype. The experimental results were supplemented by a SimuPact numerical model as well as an analytical model to reduce interference from invasive telemetry, validate the numerical model, and prompt follow-up parametric numerical studies for design optimization. The micro gas turbine generated a steady-state electrical output of 0.145 kWe at a fuel flow rate of 13.1 slpm. Based on the numerical simulation, the turbine ran at an isentropic efficiency of 57 % and a compressor isentropic efficiency of 71 % at an air mass flow rate of 72.8 g/s. The recuperator had a thermodynamic effectiveness of 80 % which was validated by analytical calculations. A secondary simple Brayton cycle test was also performed on the micro gas turbine to determine the effect of auxiliary pressure drop on the electrical performance of the micro gas turbine. Without the added pressure drop of the solar receiver, recuperator, downstream components, and combustion chamber operating at a higher inlet temperature, the micro gas turbine electrical output increased to 0.93 kWe on average at an average fuel flow rate of 36.4 slpm. The solar collector was analysed, showing an average intercept factor of 64 %, an average receiver thermal efficiency of 29 % and collector efficiency of 17 %. Based on the performance of the power cycle at the steady-state point of interest, the receiver and collector efficiencies are estimated to increase by up to 37 % during average operating conditions and by up to 82 % during peak operating conditions in summer. Fuel savings of between 12 % and 33 % were determined for an equivalent amount of process heat generated in fuel-only conditions. Fuel savings are predicted to increase up to 52 % if the intercept factor of the reflector is improved to the design target of 90 %. Additional improvements such as increasing the reflector size or reducing the micro-gas turbine were also noted to improve fuel savings.

The test was successful as a proof of concept, however three primary challenges were identified. Firstly, the added pressure drop of the auxiliary components and combustion chamber operating at higher inlet temperature around the micro gas turbine negatively impacted the micro gas turbine's performance to such an extent that the added solar energy and recuperation was not beneficial for electrical production per slpm of fuel when compared to a simple open Brayton cycle. Secondly, the late start of the test meant that steady state was achieved during the late afternoon where a sub-optimal direct normal irradiance was present, and the elevation angle was low which negatively impacted the solar collector efficiency. Thirdly, the inadequate calibration of the reflector led to a relatively low collector intercept factor further impacting the collector performance.

Based on the initial study of the Solar Turbo Combined Heat and Power prototype some important recommendations can be made:

- Longer micro gas turbine run time is required to ensure integrity of the operation at different elevation angles during solar tracking. The turbine and compressor should be designed to operate at the higher elevation of Pretoria, South Africa (with lower inlet air pressure to the compressor) than in the United Kingdom (closer to sea-level).
- Heat loss should be minimised by incorporating more stringent insulating methods around the hot surfaces of the power cycle. The temperature is estimated to have dropped from 556 K at the outlet of the hot recuperator to 465 K measured at the inlet of the thermal energy storage unit. An estimated 7 kW of heat loss from the available 19 kW of process air was off-gassed (37 % of the off-gassed heat from the recuperator hot outlet). The direct impact of the heat loss is certainly present between the receiver outlet and the combustion chamber inlet with an estimated 580 W lost to the ambient (23 % of the net heat captured by the receiver).
- Pressure drop through auxiliary components added to the micro gas turbine should be minimized to improve the plant's performance in a holistic sense. Larger cross-sectional areas should be used at valve connections, the combustion chamber inlet, as well as in the recuperator. The combustion chamber design should also be improved to minimize pressure drop while maintaining thermal performance.
- The optical performance of the faceted solar reflector can be improved by performing more stringent optical calibration methods such as moonlight testing (or an alternative day time calibration method). This should be done in addition to actively controlling the facets' membrane depths throughout the day by adjusting the vacuum pressure within the plenum space of each facet. Alternatively, solid reflector facets should be investigated that mitigate the need for active vacuum control.
- A second-law analysis was not conducted in the current study since the results came from an initial test phase that spanned a single day with the thermal energy storage unit not reaching melting temperature during operation. It is recommended that a second-law analysis can be incorporated into a future study where the design lessons learned from this initial testing phase have been addressed.
- An experimental analysis of the Solar Turbo Combined Heat and Power prototype in solar-only mode, fuel-only mode and solar-hybrid operation would provide a broader perspective on the performance of the solar hybridized Solar Turbo Combined Heat and Power prototype. Since only solar-hybrid operation was tested during the initial study, it is recommended that the other two operational modes be included in follow-up experimental studies.
- A performance comparison between the Solar Turbo Combined Heat and Power prototype and a simple-cycle micro gas turbine was

conducted in Section 5.3. A more appropriate comparison would be achieved by investigating and comparing the Solar Turbo Combined Heat and Power prototype performance with that of a (non-hybridized) recuperated Brayton cycle and should be considered in future studies.
- A SimuPact numerical model has been calibrated based on the steady state numerical data and can be used for predicting transient behaviour of the Solar Turbo Combined Heat and Power prototype in future work.

CRediT authorship contribution statement

Jonathan K. Swanepoel: Writing – review & editing, Writing – original draft, Visualization, Validation, Software, Project administration, Methodology, Investigation, Formal analysis, Data curation, Conceptualization. **Willem G. le Roux:** Conceptualization, Methodology, Investigation, Resources, Writing – original draft, Writing – review & editing, Supervision, Project administration, Funding acquisition. **Casey Roosendaal:** Writing – review & editing, Software, Project administration, Methodology, Investigation, Formal analysis, Conceptualization. **Seyed H. Madani:** Writing – review & editing, Resources, Project administration, Methodology, Investigation, Funding acquisition, Data curation, Conceptualization. **Gideon de Wet:** Writing – review & editing, Validation, Software, Resources, Methodology, Investigation, Formal analysis. **Theoklis Nikolaidis:** Writing – review & editing, Supervision, Project administration, Methodology, Funding acquisition, Conceptualization. **Westley Roosendaal:** Software, Methodology, Investigation, Data curation. **Chase Onorati:** Writing – review & editing, Methodology, Investigation, Formal analysis. **Adriano Sciacovelli:** Writing – review & editing, Project administration, Funding acquisition, Conceptualization. **Yize Liu:** Writing – review & editing, Methodology, Investigation, Formal analysis. **Tlou S. Mokobodi:** Writing – review & editing, Methodology, Investigation, Data curation. **Duncan S. McGee:** Writing – review & editing, Methodology. **Ken J. Craig:** Writing – review & editing, Supervision.

Declaration of competing interest

The authors declare the following financial interests/personal relationships which may be considered as potential competing interests: LE ROUX WG, SWANEPOEL JK, ROOSENDAAL C, International Patent, PCT/IB2023/055974.

Data availability

Data will be made available on request.

Acknowledgements

The authors would like to acknowledge the project partners of the project “Solar-Turbo CHP, Semi-Renewable, Grid Independent Micro Combined Heat and Power System” as well as the financial support from Innovate UK of the United Kingdom (Ref: 105920), the Technology Innovation Agency (TIA) of South Africa, and the Renewable Energy Hub and Spokes Programme of the Department of Science and Innovation (DSI) of South Africa, through the UP Solar Thermal Spoke. Staff and students in the Department of Mechanical and Aeronautical Engineering at the University of Pretoria who were involved with the ST-CHP project are also greatly acknowledged.

Appendix A. Pressure drop

The pressures within the power plant were estimated by means of a dimensional analysis. Pressure drop values through the process piping and components were experimentally measured at ambient conditions at a range of mass flow rates (Reynolds numbers) and a dimensional analysis was applied by means of the Buckingham Pi Theorem [71]. The pressure drop values may then be compounded to form a total head loss between different points. The process resulted in three dimensionless groups that were required to equate between the ambient tests and the on-sun tests to achieve dynamic similarity. The three dimensionless groups are presented in Equation A–1, Equation A–2 and Equation A–3.

$$\Pi_1 = \frac{L}{D_h} \tag{A-1}$$

$$\Pi_2 = \frac{\rho V D_h}{\mu} = Re \tag{A-2}$$

$$\Pi_3 = \frac{\Delta P}{\frac{1}{2}\rho V^2} = C_P \tag{A-3}$$

The resulting pressure coefficients were modelled as a function of Reynolds number according to an exponential relationship in Equation A–4. The pressure drop during operational testing conditions were then determined by multiplying the pressure coefficient by the dynamic pressure as presented in Equation 12. Air properties were determined from the bulk fluid temperature and inlet pressure through the component. The coefficients $\bar{A}$ and $\bar{B}$ were determined through least mean squared method and are summarised in Table A–1. The inner diameter of the component was used as the characteristic length in calculating the Reynolds number. The results of this analysis were used in the analytical model for the steady-state analysis when estimating the pressure conditions in the system at operational points of interest.

$$C_P = \bar{A} Re^{\bar{B}} \tag{A-4}$$

Table A-1
Modelling coefficients for pressure coefficients of power cycle components.

State	Component	Inner diameter (mm)	$\bar{A}$	$\bar{B}$
(3–4)	Recuperator cold	50	1.87E + 5	−9.35E-1
(4–6)	Tube 1 + receiver	83	7.48E + 5	−1.12
(6–7)	Tube 2	83	5.01E + 6	−1.17
(7–8)	Combustion chamber	50	5.62E + 1	−1.71E-1

(*continued on next page*)

Table A-1 (*continued*)

State	Component	Inner diameter (mm)	$\bar{A}$	$\bar{B}$
(10–11)	Recuperator hot	50	3.75E + 1	−3.27E-1
(11–11.25)	Tube 3	83	1.07E + 2	−3.30E-1
(11.25–11.5)	Flexible hose	83	9.49E + 1	−3.31E-1
(11.5–11.75)	Tube 4	83	1.57E + 2	−3.33E-1
(11.75–12)	QTP valve	50	4.75E + 1	−3.36E-1
(12–13)	TES	83	4.05E + 1	−3.40E-1

Appendix B. Uncertainty analysis

The ISO 98–3:2008 [72] standard was used in determining and presenting uncertainties for the experimental results. Expanded uncertainties conform to a normal distribution and fall within a 95 % confidence interval or two standard deviations from the mean (k-factor of 2). Relative uncertainties are determined by taking the expanded uncertainty over the reference value. The steady-state measurement results were used as reference values for the analysis. The measurement uncertainty is summarised in Table B–1. The combined uncertainties of the system process pressures are summarised in Table B–2. The combined uncertainties of the combustion chamber heat loss and subsequent air mass flow rate are determined in Table B–3. The combined uncertainty of the receiver and collector performance characteristics are determined in Table B–4.

Table B-1
Measurement uncertainty for point of interest at 16:46 – 16:48 (30 March 2022).

Description	Value	Standard Uncertainty	Expanded Uncertainty	Relative Uncertainty
Ambient				
Ambient temperature, T_{amb} (K)	297.91	1.10	2.19	0.74 %
Ambient pressure, P_{amb} (kPa)	86.21	0.17	0.33	0.39 %
Direct normal irradiance, *DNI* (W/m^2)	610.85	4.09	4.09	0.67 %
Thermocouples				
Temperature receiver inlet, T_5 (K)	935.37	0.76	1.53	0.16 %
Temperature receiver outlet, T_6 (K)	966.49	0.92	1.85	0.19 %
Temperature turbine inlet, T_8 (K)	1183.68	2.10	4.21	0.36 %
Temperature TES inlet, T_{12} (K)	465.04	0.87	1.73	0.37 %
Temperature TES outlet, T_{13} (K)	385.03	0.87	1.73	0.37 %
MGT sensors				
Fuel flow rate, $\dot{V}_f$ (slpm)	13.10	0.35	0.70	5.33 %
MGT speed (krpm)	130	3.75	7.51	5.77 %
MGT electrical output (W)	144.46	4.17	8.34	5.77 %

Table B-2
Combined uncertainty of estimated pressures for point of interest at 16:46 – 16:48 (30 March 2022).

Description	Value	Standard Uncertainty	Expanded Uncertainty	Relative Uncertainty
Pressure coefficient from ambient pressure tests	–	–	–	27.15 %
Compressor outlet, P_2 (kPa)	200.45	3.16	6.33	3.16 %
Recuperator cold inlet, P_3 (kPa)	200.45	3.16	6.33	3.16 %
Recuperator cold outlet, P_4 (kPa)	195.94	3.05	6.09	3.11 %
Receiver inlet, P_5 (kPa)	195.94	3.05	6.09	3.11 %
Receiver outlet, P_6 (kPa)	194.86	3.04	6.08	3.12 %
Combustion inlet, P_7 (kPa)	190.58	2.93	5.86	3.07 %
Turbine inlet, P_8 (kPa)	175.34	0.48	0.97	0.55 %
Turbine outlet, P_9 (kPa)	90.85	0.48	0.97	1.06 %
Recuperator hot inlet, P_{10} (kPa)	90.85	0.48	0.97	1.06 %
Recuperator hot outlet, P_{11} (kPa)	88.94	0.32	0.64	0.72 %
TES inlet, P_{12} (kPa)	86.34	0.17	0.34	0.39 %
TES outlet, P_{13} (kPa)	86.21	0.17	0.33	0.39 %

Table B-3
Combined uncertainty of combustion chamber and air mass flow rate for point of interest 16:46 – 16:48 (30 March 2022).

Description	Value	Standard Uncertainty	Expanded Uncertainty	Relative Uncertainty
Combustion chamber heat loss				
Estimated temperature of combustion chamber outer surface, $T_{comb,2}$ (K)	1566.31	350.36	700.72	44.74 %
Insulation inner diameter, $D_{ins,i}$ (m)	0.0870	0.0006	0.0012	1.33 %
Insulation outer diameter, $D_{ins,o}$ (m)	0.1870	0.0058	0.0115	6.17 %
Insulation length, L_{ins} (m)	0.3000	0.0058	0.0115	3.85 %
Insulation outer area, $A_{s,o}$ (m^2)	0.1762	0.0064	0.0128	7.28 %

(*continued on next page*)

Table B-3 (*continued*)

Description	Value	Standard Uncertainty	Expanded Uncertainty	Relative Uncertainty
Outer combustion chamber conduction resistance, R_{cond} (K/W)	2.84	0.13	0.26	9.11 %
Outer combustion chamber convection resistance, R_{conv} (K/W)	0.66	0.02	0.05	7.28 %
Outer combustion chamber radiation resistance, R_{rad} (K/W)	0.58	0.02	0.04	7.28 %
Combustion chamber total thermal resistance, R_{comb} (K/W)	3.15	0.13	0.26	8.23 %
Combustion chamber heat loss, $\dot{Q}_{loss,comb}$ (W)	403.17	112.60	225.19	55.86 %
Air mass flow rate				
Density of LPG @ STP (kg/m^3)	2.03	0.0012	0.0023	0.12 %
Propane viscosity @ STP (Pa.s)	8.15E-6	2.35E-7	4.70E-7	5.77 %
LPG viscosity STP (Pa.s)	7.84E-6	2.26E-7	4.53E-7	5.77 %
LPG fuel flow rate (kg/s)	4.26E-4	2.08E-5	4.16E-5	9.78 %
Heat of combustion (kW)	19.49	0.95	1.91	9.78 %
Heat loss from combustion chamber + flanges (kW)	0.81	0.11	0.23	27.80 %
Net heat of combustion (kW)	18.68	0.96	1.92	10.27 %
Air mass flow rate (kg/s)	0.0722	0.0048	0.010	13.22 %

Table B-4
Combined uncertainty of collector and receiver for point of interest 16:46 – 16:48 (30 March 2022).

Description	Value	Standard Uncertainty	Expanded Uncertainty	Relative Uncertainty
Receiver				
Enthalpy before receiver, h_5 (J/kg)	1,099,229	6410	12,819	1.17 %
Enthalpy after receiver, h_6 (J/kg)	1,134,439	6639	13,278	1.17 %
Net heat gain from receiver (kW)	2.54	0.69	1.37	54.06 %
Convection heat loss (kW)	2.70	0.29	0.58	21.34 %
Receiver total heat loss (kW)	6.53	0.29	0.58	8.84 %
Intercepted heat (kW)	9.07	0.75	1.49	16.43 %
Collector				
Solar heat available (kW)	15.06	0.10	0.20	1.34 %
Reflected heat (kW)	13.55	0.09	0.18	1.34 %
Intercept factor	67 %	5.52 %	11.04 %	16 %
Receiver efficiency	28 %	7.92 %	15.83 %	56 %
Collector efficiency	17 %	4.57 %	9.13 %	54 %

Appendix C. Detailed heat loss analytical model

Process piping heat loss was determined from Equation C-1 to Equation C-4 [73]. The thermal conductivity of the stainless-steel tubing was determined as a linear function of temperature according to the data tables in Çengel and Ghajar [73]. The thermal conductivity of the insulation blanket used to insulate the combustion chamber and process piping was provided as a function of temperature according to Refraline (Pty) Ltd [74].

The internal forced convection heat transfer coefficient for fully developed turbulent flow was determined through the correlation of Gnielinski [75]. The friction factor for internal flow was determined iteratively through the Colebrook equation [76]. Air properties were determined at bulk fluid temperature throughout the entire length of the tube sections. Surface roughness of the rubber hose between state 2 and state 3 was assumed to be 0.05 mm [77]. The roughness of the 316 stainless-steel tubing was assumed to be 0.045 mm [73].

External convection heat loss from the outer insulation surfaces were determined as a combination of natural and forced convection according to Equation C-3 [73]. Natural convection was determined by assuming all piping as being horizontal [78]. Air properties were determined at film temperature for all external convection calculations. External forced convection from the piping was determined according to Churchill and Bernstein [79]. Radiation heat loss from the insulation surfaces was determined using a thermal emissivity of 0.9 [80].

The 316 stainless-steel flange connections, connecting the piping to all the primary components were 60 mm long (each flange was roughly 25 mm thick with a 10 mm gasket), had an inner diameter of 83 mm and an outer diameter of 190 mm. No insulation covered these connections, and their heat loss was considered according to Equation C-4 [73]. Convection heat loss to the ambient environment was analysed by taking the convective surface to be the exposed outer surface area of the two-flange connections (including faces and outer diameters). The radiation surface area was taken as the exposed outer diameter surface area of the two connecting flanges and the thermal emissivity was taken to be that of an “as-received” 316 stainless steel surface (0.25 at 400 K and 0.37 at 1000 K) [81]. The internal convection resistance of the flange was determined based on Gnielinski [75] and the Colebrook [73] equations. Air properties for internal forced convection were determined at the process state of each connection (see Fig. 1). The external convection resistance at the flange outer diameter surface area was determined using Equation C-4. The forced convection resistance at the faces of the flange connections were determined using the correlation given in Cengel and Ghajar [73] and the natural convection resistance of the flat surfaces were determined using the correlation of Churchill and Chu [82].

$$\dot{Q}_{loss,i|i+1} = \frac{T_{air} - T_{amb}}{R_{tot}} \tag{C-1}$$

$$R_{tot} = \frac{1}{\widehat{h}_i A_{s,i}} + \frac{\ln\left(D_{tube,o}/D_{tube,i}\right)}{2\pi L_{tube} k_{tube}} + \frac{\ln\left(D_{ins,o}/D_{ins,i}\right)}{2\pi L_{ins} k_{ins}} + \left[\left(\frac{1}{\widehat{h}_o A_{s,o}}\right)^{-1} + \left(\varepsilon\sigma A_{s,o}\left(T_o^2 + T_{amb}^2\right)\left(T_o + T_{amb}\right)\right)^{-1}\right]^{-1} \tag{C-2}$$

$$Nu_o = \left(Nu_{forced}^{3.5} + Nu_{natural}^{3.5}\right)^{\frac{1}{3.5}} \tag{C-3}$$

$$R_{tot,flange} = \frac{1}{\widehat{h}_i A_{s,i}} + \frac{\ln\left(D_{tube,o}/D_{tube,i}\right)}{2\pi L_{tube} k_{tube}} + \left[\begin{array}{c}\left(\frac{1}{\widehat{h}_{face} A_{face}}\right)^{-1} \\ + \left(\frac{1}{\widehat{h}_{OD} A_{OD}}\right)^{-1} \\ + \left(\varepsilon\sigma A_{OD}\left(T_{OD}^2 + T_{amb}^2\right)\left(T_{OD} + T_{amb}\right)\right)^{-1}\end{array}\right]^{-1} \tag{C-4}$$

Appendix D. Recuperator detailed analysis

The recuperator cold side inlet temperature was estimated using Equation 11 and considering the process piping heat loss between state 2 and state 3 (see Fig. 1). The recuperator cold side outlet temperature was estimated using the measured inlet temperature of the receiver and considering the process piping heat loss between state 4 and state 5. The recuperated heat ($\dot{Q}_{recup}$) was then determined from the enthalpy change across the cold side of the recuperator. The hot side outlet temperature was initially estimated, and the recuperated heat (and recuperator heat loss) was then used to determine the inlet temperature of the recuperator hot side. All air properties were determined at bulk fluid temperature.

The recuperator NTU and subsequent effectiveness were then determined from the perspective of recuperator geometry (see Equation D–1 to Equation D–6 and Table D–1). The micro-channel Nusselt number was determined from a table detailing fully developed, laminar flow in tubes (see Table 8-1 in Çengel and Ghajar [73]) for a rectangular cross-section and triangular cross-section (hot side and cold side respectively). The hydraulic diameter was determined by considering the micro-channel's cross-sectional area and perimeter using Equation D–1. An iterative process was followed to find the correct outlet temperature for the recuperator hot side which resulted in the effectiveness values reaching agreement between the temperature states and the recuperator geometry.

The recuperator used in the cycle was a stainless-steel flat plate counterflow heat exchanger. The properties of the recuperator are summarized in Table 3. The geometric properties of the recuperator may be used to validate the recuperator effectiveness found in the SimuPact simulation results through the NTU-effectiveness method in Table D–1. Air properties are determined from the bulk fluid temperature and average pressure per side.

$$D_{h,mchannel} = \frac{4A_{c,mchannel}}{p_{mchannel}} \tag{D-1}$$

$$(UA_s)_{mchannel} = \frac{Nu_{mchannel} k_{mchannel}}{D_{h,mchannel}} A_{s,mchannel} \tag{D-2}$$

$$(UA_s)_{channel} = N_{mchannel} \times (UA_s)_{mchannel} \tag{D-3}$$

$$(UA_s)_{side} = N_{channel} \times (UA_s)_{channel} \tag{D-4}$$

$$NTU = \frac{(UA_s)_{side}}{C_{min}} \tag{D-5}$$

$$\breve{\varepsilon} = \frac{1 - e^{-NTU(1-c)}}{1 - ce^{-NTU(1-c)}} \tag{D-6}$$

It is evident that both the recuperator effectiveness found by the geometry analysis and the effectiveness found by the SimuPact simulation are comparable within 0.5 % difference. The thermal resistance of the cold side is 305 % larger than that of the hot side restricting the heat transfer rate through the recuperator. This may be due to the selection of micro-channel and fin geometry which resulted in a hot channel heat transfer area 62 % larger than that of the cold side and a hot channel heat transfer coefficient 163 % larger than that of the cold side. However, the heat exchanger design had to also limit the pressure drop through the channel while maximizing heat transfer.

Table D-1
Summary of heat exchanger analysis using NTU-effectiveness method for point of interest at 16:46 – 16:48 (30 March 2022).

Description	High Pressure / Cold Side	Low Pressure / Hot Side
Mass flow rate		
Side mass flow rate (kg/s)	7.22E-2	7.22E-2
Channel mass flow rate (kg/s)	1.24E-3	1.29E-3

(*continued on next page*)

Table D-1 (*continued*)

Description	High Pressure / Cold Side		Low Pressure / Hot Side
Micro channel analysis	**Core**	**Divider**	
Micro channel heat transfer area (m^2)	3.1E-3	1.14E-3	1.94E-3
Micro channel cross sectional area (m^2)	2.14E-5	8.55E-6	5.5E-6
Micro channel perimeter (m)	3.04E-2	1.29E-2	1.08E-2
Micro channel hydraulic diameter (m)	2.81E-3	2.65E-3	2.05E-3
Micro channel mass flow rate (kg/s)	1.38E-4	5.31E-5	1.28E-5
Micro channel Reynolds number (-)	545.00	494.16	125.63
Micro channel characteristic dimension *	138.39°	92.94°	2.91
Micro channel Nusselt number (-) *	2.68	2.98	4.79
Heat transfer factor (W/K)	0.15	0.06	0.26
Channel analysis			
Heat transfer area (m^2)	0.12		0.20
Heat transfer factor (W/K)	6.33		26.52
Side analysis			
Heat transfer area (m^2)	6.99		10.83
Heat transfer factor (W/K)	367.10		1485.04
Thermal resistance (K/W)	0.0027		0.0007
Overall analysis			
Total heat transfer area (m^2)	10.83		
Total thermal resistance (K/W)	0.0034		
Overall heat transfer coefficient (W/m^2K)	27.17		
NTU (-)	3.81		
Effectiveness	80.15 %		
Effectiveness from SimuPact simulation	79.83 %		

* Table 8-1, Çengel and Ghajar [73]

References

[1] IRENA, "World Energy Transition Outlook 2023: 1.5 C Pathway," International Renewable Energy Agency, Abu Dhabi, 2023, vol. 1.

[2] M.T. Islam, N. Huda, A. Abdullah, R. Saidur, A comprehensive review of state-of-the-art concentrating solar power (CSP) technologies: Current status and research trends, Renewable and Sustainable Energy Reviews 91 (2018) 987–1018.

[3] R. Thonig, A. Gilmanova, and J. Lilliestam. *CSP.guru 2023-07-01*. [Online]. Available: DOI: 10.5281/zenodo.1318151.

[4] S. Akar, P. Kurup, M. Boyd, E. Wachs, and C. McMillan, "Renewable Thermal Energy Systems: Modeling Developments and Future Directions (Report 3)," United States, 2023. [Online]. Available: https://www.osti.gov/biblio/1957772.

[5] J. Cresko *et al.*, "DOE Industrial Decarbonization Roadmap," USDOE Office of Energy Efficiency and Renewable Energy (EERE), 2022.

[6] M. Abuseada, T.S. Fisher, Continuous solar-thermal methane pyrolysis for hydrogen and graphite production by roll-to-roll processing, Applied Energy 352 (2023) 121872, https://doi.org/10.1016/j.apenergy.2023.121872.

[7] SolarPACES. "CSP Projects Around the World." www.solarpaces.org (accessed 06 March, 2023).

[8] A. Giovannelli, State of the art on small-scale concentrated solar power plants, Energy Procedia 82 (2015) 607–614, https://doi.org/10.1016/j.egypro.2015.12.008.

[9] Z. Kee, Y. Wang, J. Pye, A. Rahbari, Small-scale concentrated solar power system with thermal energy storage: System-level modelling and techno-economic optimisation, Energy Conversion and Management 294 (2023) 117551, https://doi.org/10.1016/j.enconman.2023.117551.

[10] A. Algieri, P. Morrone, Thermo-economic investigation of solar-biomass hybrid cogeneration systems based on small-scale transcritical organic Rankine cycles, Applied Thermal Engineering 210 (2022) 118312, https://doi.org/10.1016/j.applthermaleng.2022.118312.

[11] D. Mills, Advances in solar thermal electricity technology, Solar Energy 76 (1) (2004) 19–31, https://doi.org/10.1016/S0038-092X(03)00102-6.

[12] J. Coventry, C. Andraka, Dish systems for CSP, Solar Energy 152 (2017) 140–170.

[13] L. Aichmayer, J. Garrido, B. Laumert, Thermo-mechanical solar receiver design and validation for a micro gas-turbine based solar dish system, Energy 196 (2020) 116929, https://doi.org/10.1016/j.energy.2020.116929.

[14] W.G. Le Roux, T. Bello-Ochende, J.P. Meyer, The efficiency of an open-cavity tubular solar receiver for a small-scale solar thermal Brayton cycle, Energy Conversion and Management 84 (2014) 457–470, https://doi.org/10.1016/j.enconman.2014.04.048.

[15] W.G. Le Roux, A. Sciacovelli, Recuperated solar-dish Brayton cycle using turbocharger and short-term thermal storage, Solar Energy 194 (2019) 569–580, https://doi.org/10.1016/j.solener.2019.10.081.

[16] W.G. Le Roux, Thermodynamic optimisation and experimental collector of a dish-mounted small-scale solar thermal Brayton cycle, University of Pretoria, Pretoria, South Africa, 2015.

[17] B. Dickey, Test results from a concentrated solar microturbine Brayton cycle integration, in: Turbo Expo: Power for Land, Sea, and Air, Vol. 54631, 2011, pp. 1031–1036, https://doi.org/10.1115/GT2011-45918.

[18] R. Korzynietz, et al., Solugas – Comprehensive analysis of the solar hybrid Brayton plant, Solar Energy 135 (2016) 578–589, https://doi.org/10.1016/j.solener.2016.06.020.

[19] M. Quero, R. Korzynietz, M. Ebert, A. Jiménez, A. del Río, and J. Brioso, "Solugas – Operation experience of the first solar hybrid gas turbine system at MW scale," presented at the SolarPACES 2013 conference, Las Vegas, USA, 2013.

[20] Sandia National Laboritories, "Parabolic dish module experiment. Final test report," Albuquerque, NM, United States, SAND-85-7007, 1986. [Online]. Available: https://www.osti.gov/biblio/6054022.

[21] L.D. Jaffe, Test results on parabolic dish concentrators for solar thermal power systems, Solar Energy 42 (2) (1989) 173–187, https://doi.org/10.1016/0038-092X(89)90144-8.

[22] Garret Energy Company, "Brayton cycle solarized advanced gas turbine final report," DOE/NASA/0181, 1986.

[23] ETN Global. "OMSoP." https://etn.global/ (accessed 15 March, 2023).

[24] M. Lanchi, et al., Investigation into the coupling of micro gas turbines with CSP technology: OMSoP project, Energy Procedia 69 (2015) 1317–1326, https://doi.org/10.1016/j.egypro.2015.03.146.

[25] W. Wang, G. Ragnolo, L. Aichmayer, T. Strand, B. Laumert, Integrated design of a hybrid gas turbine-receiver unit for a solar dish system, Energy Procedia 69 (2015) 583–592, https://doi.org/10.1016/j.egypro.2015.03.067.

[26] G. Ragnolo, L. Aichmayer, W. Wang, T. Strand, B. Laumert, Technoeconomic design of a micro gas-turbine for a solar dish system, Energy Procedia 69 (2015) 1133–1142, https://doi.org/10.1016/j.egypro.2015.03.182.

[27] L. Aichmayer, J. Spelling, B. Laumert, Thermoeconomic analysis of a solar dish micro gas-turbine combined-cycle power plant, Energy Procedia 69 (2015) 1089–1099, https://doi.org/10.1016/j.egypro.2015.03.217.

[28] W. Wang, B. Wang, L. Li, B. Laumert, T. Strand, The effect of the cooling nozzle arrangement to the thermal performance of a solar impinging receiver, Solar Energy 131 (2016) 222–234, https://doi.org/10.1016/j.solener.2016.02.052.

[29] W. Wang, B. Laumert, Effect of cavity surface material on the concentrated solar flux distribution for an impinging receiver, Solar Energy Materials and Solar Cells 161 (2017) 177–182, https://doi.org/10.1016/j.solmat.2016.12.008.

[30] L. Aichmayer, J. Garrido, W. Wang, B. Laumert, Experimental evaluation of a novel solar receiver for a micro gas-turbine based solar dish system in the KTH high-flux solar simulator, Energy 159 (2018) 184–195, https://doi.org/10.1016/j.energy.2018.06.120.

[31] City University of London, "Final Report Summary - OMSOP (Optimised Microturbine Solar Power system)," European Union, Luxembourg, 213872, 2018. [Online]. Available: https://cordis.europa.eu/project/id/308952/reporting.

[32] W. Wang, A. Malmquist, B. Laumert, "Comparison of potential control strategies for an impinging receiver based dish-Brayton system when the solar irradiation exceeds its design value," (in eng), Energy Conversion and Management 169 (2018) 1–12, https://doi.org/10.1016/j.enconman.2018.05.045.

[33] L. Aichmayer, J. Garrido, B. Laumert, Scaling effects of a novel solar receiver for a micro gas-turbine based solar dish system, Solar Energy 162 (2018) 248–264, https://doi.org/10.1016/j.solener.2018.01.020.

[34] M. Lanchi, J. Al-Zaili, V. Russo, M. Falchetta, M. Montecchi, L. Aichmayer, A quasi-steady state model of a solar parabolic dish micro gas turbine demonstration plant, Energies 15 (3) (2022) 1059. https://www.mdpi.com/1996-1073/15/3/1059.

[35] J. Kesseli and E. Vollnogle, "Brayton Power Conversion System," Brayton Energy LLC, DE-FC36-08GO18029/A000, 2011.

[36] W.G. Le Roux, J.P. Meyer, Modeling the small-scale dish-mounted solar thermal Brayton cycle, in: AIP Conference Proceedings, vol. 1734, no. 1, 2016, https://doi.org/10.1063/1.4949144.
[37] T.M. Wolff, W.G. Le Roux, J.P. Meyer, Heat loss analysis for an open-cavity tubular solar receiver, in: International Heat Transfer Conference Digital Library, Begel House Inc, 2018, pp. 7695–7702, https://doi.org/10.1615/IHTC16.nee.024010.
[38] K.J. Craig, M. Slootweg, W.G. Le Roux, T.M. Wolff, J.P. Meyer, Using CFD and ray tracing to estimate the heat losses of a tubular cavity dish receiver for different inclination angles, Solar Energy 211 (2020) 1137–1158, https://doi.org/10.1016/j.solener.2020.10.054.
[39] C. Roosendaal, J.K. Swanepoel, W.G. Le Roux, Performance analysis of a novel solar concentrator using lunar flux mapping techniques, Solar Energy 206 (2020) 200–215, https://doi.org/10.1016/j.solener.2020.05.050.
[40] C. Roosendaal, J. K. Swanepoel, W.G. Le Roux, Optical modelling of a vacuum-membrane solar dish based on elliptical television antenna, South African Sustainable Energy Conference (SASEC), Lanzerac Wine Estate, Western Cape, 2021.
[41] J.K. Swanepoel, C. Roosendaal, W.G.L. Roux, Photogrammetry analysis of a vacuum-membrane solar dish using elliptical television antennas, in: AIP Conference Proceedings, Vol. 2445, No. 1, AIP Publishing, 2022, p. 120021, https://doi.org/10.1063/5.0087025.
[42] W. G. Le Roux, C. Roosendaal, and J. K. Swanepoel, "Solar Collector," (in English), International Patent PCT/IB2023/055974, 2023. [Online]. Available: www.wipo.int.
[43] I. Reda, A. Andreas, "Solar position algorithm for solar radiation applications (revised)", National Renewable Energy Lab (NREL), Golden, CO (united States), 2008.
[44] Sundog Solar Technology. "EverBright Mirror Film." www.sundogsolartech.com (accessed 20 March, 2023).
[45] NAVIS elektronika. "NAVIS anemometers." www.navis-anemometers.com/ (accessed 20 March, 2023).
[46] Samad Power Ltd. "Turbogenerator." https://samad-power.co.uk/ (accessed 21 August, 2023).
[47] Y. Liu, T. Nikolaidis, A. Gamil, S. H. Madani, and M. Sarkandi, "Combustor Development and Performance Analysis for Recuperated Microturbine Application," in *AIAA Propulsion and Energy 2021 Forum*.
[48] G. Humbert, C. Roosendaal, J.K. Swanepoel, H.M. Navarro, W.G. Le Roux, A. Sciacovelli, Development of a latent heat thermal energy storage unit for the exhaust of a recuperated solar-dish Brayton cycle, Applied Thermal Engineering 216 (2022) 118994, https://doi.org/10.1016/j.applthermaleng.2022.118994.
[49] M.J. Brooks, et al., SAURAN: A new resource for solar radiometric data in Southern Africa, Journal of Energy in Southern Africa 26 (1) (2015) 2–10.
[50] Simgenics LLC. "SimuPACT." https://simgenics.com/ (accessed 06 July, 2023).
[51] G. J. De Wet, W. G. Le Roux, S. H. Madani, A. Azadi, S. Hosseini, and K. J. Craig, "Transient modelling of solar-gas hybrid brayton cycle for prototype experimental setup," in *SASEC*, Stellenbosch, South Africa, 2021. Available at: https://sasec.org.za/.
[52] AFROX. "Liquid Petrolium Gas (LPG) Product Reference Manual Section 5." www.afrox.co.za (accessed 19 October, 2022).
[53] I.H. Bell, J. Wronski, S. Quoilin, V. Lemort, Pure and pseudo-pure fluid thermophysical property evaluation and the open-source thermophysical property library CoolProp, Industrial and Engineering Chemistry Research 53 (6) (2014) 2498–2508, https://doi.org/10.1021/ie4033999.
[54] Refraline (Pty) Ltd, "Data sheet - ceramic fibre board," 10 01 2023 2023. [Online]. Available: www.refraline.com.
[55] R.D. Jilte, S.B. Kedare, J.K. Nayak, Natural convection and radiation heat loss from open cavities of different shapes and sizes used with dish concentrator, Mechanical Engineering Research. 3 (1) (2013), https://doi.org/10.5539/mer.v3n1p25.
[56] C. Isetti, E. Nannei, Influence of surface treatments on the total normal emittance of AISI316 stainless steel, Wärme-Und Stoffübertragung 14 (3) (1980) 211–215.
[57] R.H. Bogaard, P.D. Desai, H.H. Li, C.Y. Ho, Thermophysical properties of stainless steels, Thermochimica Acta 218 (1993) 373–393, https://doi.org/10.1016/0040-6031(93)80437-F.
[58] E. Abbasi-Shavazi, J.F. Torres, G. Hughes, J. Pye, Experimental correlation of natural convection losses from a scale-model solar cavity receiver with non-isothermal surface temperature distribution, Solar Energy 198 (2020) 355–375.
[59] S.-Y. Wu, L. Xiao, Y.-R. Li, Effect of aperture position and size on natural convection heat loss of a solar heat-pipe receiver, Applied Thermal Engineering 31 (14–15) (2011) 2787–2796.
[60] R. Y. Ma, "Wind effects on convective heat loss from a cavity receiver for a parabolic concentrating solar collector," Sandia National Lab.(SNL-NM), Albuquerque, NM (United States); California, 1993.
[61] J. K. Swanepoel, W. G. Le Roux, C. Roosendaal, and J. Buys. (2023). Heat loss analysis of an open-cavity tubular receiver for a solar-dish Brayton cycle [(Unpublished)].
[62] A.L. London, W.M. Kays, The liquid-coupled indirect-transfer regenerator for gas-turbine plants, Transactions of the American Society of Mechanical Engineers 73 (5) (2022) 529–540, https://doi.org/10.1115/1.4016310.
[63] W.M. Kays, A.L. London, Compact heat exchangers, 3rd ed., McGraw-Hill Ryerson, 1984.
[64] D.S. McGee, W. Roosendaal, W.G. Le Roux, Environmental investigation of vacuum-membrane solar-dish facets, in: AIP Conference Proceedings, vol. 2815, no. 1, 2023, https://doi.org/10.1063/5.0149745.
[65] B.L. Butler, K.J. Beninga, Focus control system for stretched-membrane mirror module, Google Patents (1991).
[66] P. Schertz, D. Brown, and A. Konnerth III, "Facet development for a faceted stretched-membrane dish by Solar Kinetics, Inc," Sandia National Lab. (SNL-NM), Albuquerque, NM (United States); (1991).
[67] Sandia National Laboritories, "Facet development for a faceted stretched-membrane dish by SAIC," Albuquerque, NM, United States, 1991. [Online]. Available: https://www.osti.gov/biblio/5975800.
[68] K. Padmanathan, U. Govindarajan, V.K. Ramachandaramurthy, B. Jeevarathinam, Integrating solar photovoltaic energy conversion systems into industrial and commercial electrical energy utilization—A survey, Journal of Industrial Information Integration 10 (2018) 39–54, https://doi.org/10.1016/j.jii.2018.01.003.
[69] S. Kurtz, et al., Historical analysis of champion photovoltaic module efficiencies, IEEE Journal of Photovoltaics 8 (2) (2018) 363–372.
[70] W.G. Le Roux, Feasibility study of a hybrid small-scale dish-mounted solar thermal Brayton cycle with cogeneration, in: International Heat Transfer Conference Digital Library, Begel House Inc, 2018, pp. 7929–7936, https://doi.org/10.1615/IHTC16.nee.024185.
[71] E. Buckingham, On physically similar systems; illustrations of the use of dimensional equations, Physical Review. 4 (4) (1914) 345–376, https://doi.org/10.1103/PhysRev.4.345.
[72] ISO Guide 98-3:2008, Uncertainty of measurement-Part 3: Guide to the expression of uncertainty in measurement, International Organization for Standardization, Geneva, Switzerland, 2008.
[73] Y.A. Çengel, A.J. Ghajar, Heat and mass transfer: Fundamentals and applications, 5th ed., McGraw-Hill Education, New York, NY, United States, 2014.
[74] Refraline (Pty) Ltd. "Technical data sheet ceramic fibre blankets." www.refraline.com (accessed 09 February, 2022).
[75] V. Gnielinski, New equations for heat and mass transfer in turbulent pipe and channel flow, Int. Chem. Eng. 16 (2) (1976) 359–368.
[76] C.F. Colebrook, et al., Correspondence. turbulent flow in pipes, with particular reference to the transition region between the smooth and rough pipe laws. (includes plates), Journal of the Institution of Civil Engineers 12 (8) (1939) 393–422.
[77] S. M. Hall, "4.8 Friction Factor," in *Rules of Thumb for Chemical Engineers (6th Edition)*: Elsevier.
[78] S.W. Churchill, H.H. Chu, Correlating equations for laminar and turbulent free convection from a horizontal cylinder, International Journal of Heat and Mass Transfer 18 (9) (1975) 1049–1053.
[79] S. Churchill and M. Bernstein, "A correlating equation for forced convection from gases and liquids to a circular cylinder in crossflow," 1977.
[80] J.M. Jones, P.E. Mason, A. Williams, A compilation of data on the radiant emissivity of some materials at high temperatures, Journal of the Energy Institute 92 (3) (2019) 523–534, https://doi.org/10.1016/j.joei.2018.04.006.
[81] R.V. Tompson Jr, T.K. Ghosh, S.K. Loyalka, H. Jo, D.S. Viswanath, Long-term prediction of emissivity of structural materials for high temperature reactor systems, Univ. of Missouri, Columbia, MO (United States), 2018.
[82] S.W. Churchill, H.H. Chu, Correlating equations for laminar and turbulent free convection from a vertical plate, International Journal of Heat and Mass Transfer 18 (11) (1975) 1323–1329.